2011

CFD analysis of combustion instability for a rocket injector

Douglass W. Casey

CFD ANALYSIS OF COMBUSTION INSTABILITY FOR A ROCKET INJECTOR

by

DOUGLASS W CASEY

A THESIS

Submitted in partial fulfillment of the requirements
for the degree of Master of Science in Engineering
in
The Department of Mechanical and Aerospace Engineering
to
The School of Graduate Studies
of
The University of Alabama in Huntsville

HUNTSVILLE, ALABAMA

2011

In presenting this thesis in partial fulfillment of the requirements for a master's degree from The University of Alabama in Huntsville, I agree that the Library of this University shall make it freely available for inspection. I further agree that permission for extensive copying for scholarly purposes may be granted by my advisor or, in his/her absence, by the Chair of the Department or the Dean of the School of Graduate Studies. It is also understood that due recognition shall be given to me and to The University of Alabama in Huntsville in any scholarly use which may be made of any material in this thesis.

Douglass W Casey — 11/7/11 (date)

THESIS APPROVAL FORM

Submitted by Douglass W Casey in partial fulfillment of the requirements for the degree of Master of Science in Engineering in Mechanical Engineering and accepted on behalf of the Faculty of the School of Graduate Studies by the thesis committee.

We, the undersigned members of the Graduate Faculty of The University of Alabama in Huntsville, certify that we have advised and/or supervised the candidate of the work described in this thesis. We further certify that we have reviewed the thesis manuscript and approve it in partial fulfillment of the requirements for the degree of Master of Science in Engineering in Mechanical Engineering.

Dr. Kader Frendi	11/4/11 (Date)	Committee Chair
Dr. Robert Frederick	11/4/11 (Date)	
Dr. Babak Shotorban	11/5/11 (Date)	
Dr. Keith Hollingsworth	11/7/11 (Date)	Department Chair
Dr. Shankar Mahalingam	11/08/11 (Date)	College Dean
Dr. Rhonda K. Gaede	11/29/11 (Date)	Graduate Dean

ABSTRACT

School of Graduate Studies
The University of Alabama in Huntsville

Degree Masters of Science in Engineering College/Dept. Engineering/Mechanical and Aerospace Engineering

Name of Candidate Douglass W Casey

Title CFD Analysis of Combustion Instability for a Rocket Injector

Incorporating computational fluid dynamics (CFD) analysis alongside experiments could yield insights into High-frequency combustion instabilities (HFCI) that would otherwise be difficult to gain. Using the CFD code Loci-CHEM and a one-step methane-oxygen combustion reaction model, a preliminary analysis was conducted of a HFCI experiment for a liquid rocket engine injector. A single shear-coaxial injector ran in an open cylindrical, acoustic chamber to study HFCI excited from injector-chamber coupling. The experiment was part of an injector testing methodology at the University of Alabama in Huntsville Propulsion Research Center (PRC). The injector's axisymmetric positioning and geometry made this an ideal test case for CFD. The CFD analysis showed a dominant frequency of 2132 Hz, which corresponded to the first radial mode and agreed well with the experimental data.

Abstract Approval: Committee Chair 11/5/11
Dr. Kader Frendi

Department Chair 11/7/11
Dr. Keith Hollingsworth

Graduate Dean Rhonda Kay Haede 11/29/11
Dr. Rhonda K. Haede

ACKNOWLEDGMENTS

The National Aeronautics and Space Administration Constellation University Institutes Project provided the initial funding for this study.

My advisor, Dr. Kader Frendi, provided guidance on good practice for combustion and acoustic modeling and showed great patience during my work. My thesis committee helped me make this thesis text a much better, and hopefully more useful, document than it would have been otherwise. Scott Tashakkor, Dr. Francisco Canabal, and Dr. Ed Luke gave me extensive help with using Loci-CHEM and SolidMesh. My colleagues at the UAH Propulsion Research Center were a tremendous help in understanding the experiment better and in getting the data and measurements needed for the modeling, especially Shawn Ikard and Brian Sweeny.

It would be very difficult for me to adequately thank my family, friends, teachers, and church families spread over several states. Without their many years of encouragement, support, and guidance, I doubt I would be pursuing a dream to become a "real rocket scientist". They invested their time and energy into me, and many have long suffered my absence as I pursue my goals. Newton's comment is indeed true in my context: "If I have seen further it is only by standing on the shoulders of giants." I would not be where I am today without the efforts of others.

God gives us each a purpose and role in life. If I have any ability, opportunity, dream, or accomplishment, they are a gift from Him.

Soli Deo gloria

TABLE OF CONTENTS

LIST OF FIGURES

FIGURE PAGE

LIST OF TABLES

TABLE PAGE

LIST OF SYMBOLS

SYMBOL	DEFINITION
A_{outer}	outer surface area of flame
A_r	Arrhenius frequency factor
a	speed of sound
$\widetilde{D}_i$	conservation diffusion flux variables tensor in the x_i direction
D_s	diffusion coefficient of species s
E	total energy
E_{internal}	internal energy
E_a	Arrhenius activation energy
F	fuel
$\widetilde{F}_i$	conservation convection flux variables tensor in the x_i direction
f	frequency, surface face subscript
h_s	enthalpy of formation of species s
i, j, k	tensor indices
j'_{mn}	nth extremum of the mth Bessel function of the first kind
k_b	backward reaction rate
k_f	forward reaction rate

L	chamber length
l, m, n	resonant mode subscripts
$\mathcal{M}_s$	molecular mass of species s
NF	number of surface faces
NR	number of reactions
NS	number of species
n_i	surface normal vector in the x_i direction
Ox	oxidizer
p	pressure
q	heat release
q_i	heat flux in the x_i direction
Q	heat of combustion
R	chamber radius
R_u	universal gas constant
r	reaction subscript
$\widetilde{S}$	source term tensor
s	species subscript
s_l	laminar flame speed
T	temperature

t	time
$\widetilde{U}$	conservation variables tensor
$\dot{V}$	volumetric flowrate
$V_s i$	species diffusion velocity of species s in the x_i direction
v_i	velocity in the x_i direction
$\dot{w}_s$	mass production rate of species s
$\widetilde{x}$	position vector
x_i	spatial component
Y_s	mass fraction of species s
X_s	species s
Γ	integration surface
Γ_c	cell surface
γ	ratio of specific heats
δ_{ij}	Kronecker delta
η	Arrhenius temperature exponent
μ	dynamic viscosity
ν	stoichiometric coefficient
ν',ν''	stoichiometric coefficient for reactant side and product side, respectively

ρ	density
ρ_s	species density of species s
τ_{ij}	stress tensor (defined in (2.3))
Ω	integration volume
Ω_c	cell volume

To my family

CHAPTER 1

INTRODUCTION

Research is what I'm doing
when I don't know what I'm doing.

—Wernher von Braun

1.1 Overview

In a combustion chamber, coupling may occur amongst chamber acoustics, variations in combustion chemistry, turbulent flowfields, and, in the case of liquid rocket engines (LREs), upstream responses, such as feedline fluctuations due to injector face pressure fluctuations. When this coupling becomes strong enough, combustion instabilities (CIs) occur and can lead to degradation of engine performance. If very strong coupling is present, pressure fluctuations rapidly escalate, and localized hotspots cause burn-through and destruction of the engine. High-frequency CIs (frequencies greater than 1000 Hz) in particular are the most destructive and have been called a "most perplexing and most common [issue] in the development of new engines" [2].

The iterative process of testing a new LRE system with various thrust chamber configurations can be very expensive. As computer performance has continued to improve over the years, computational fluid dynamics (CFD) has become an important

tool in the analysis and development of LREs; however, simulating full-scale engines becomes very memory and computationally expensive when small flowfield structures, such as turbulent vortices and flames, need to be captured. The additional requirement of resolving high-frequency chamber acoustics also requires higher-resolution grids throughout the entire computational domain and not just in areas of small flowfield structures. All these phenomena are crucially important when analyzing CI.

1.2 High-Frequency Combustion Instabilities

High-frequency combustion instabilities (HFCI) are usually associated with injector response coupling with chamber frequencies [2]. LREs often have many injectors in the combustion chamber, each responding to its local environment during operation though not independent of one another. Testing a single injector in a smaller, acoustically equivalent environment offers a couple of obvious benefits. Firstly, potential sources of observed phenomena may be more easily isolated. Secondly, having only one injector makes the CFD analysis more manageable. The regions requiring high grid density (the flame region and turbulent boundary- and shear-layers) are localized to one injector.

Cavitt et al. [3], Byrd and Frederick [4], and Huyhn et al. [5] at the University of Alabama in Huntsville (UAHuntsville) Propulsion Research Center (PRC) conducted experiments using scaled-down chambers with full-scale, LRE injectors. Dexter et al. [6] and Dranovsky et al. [7] cited like-minded efforts in Russia, and Sohn [8] cited efforts in Korea. The UAHuntsville PRC methodology used a single element injector fired into an instrumented cylinder that was open to the atmosphere (Figure 1.1).

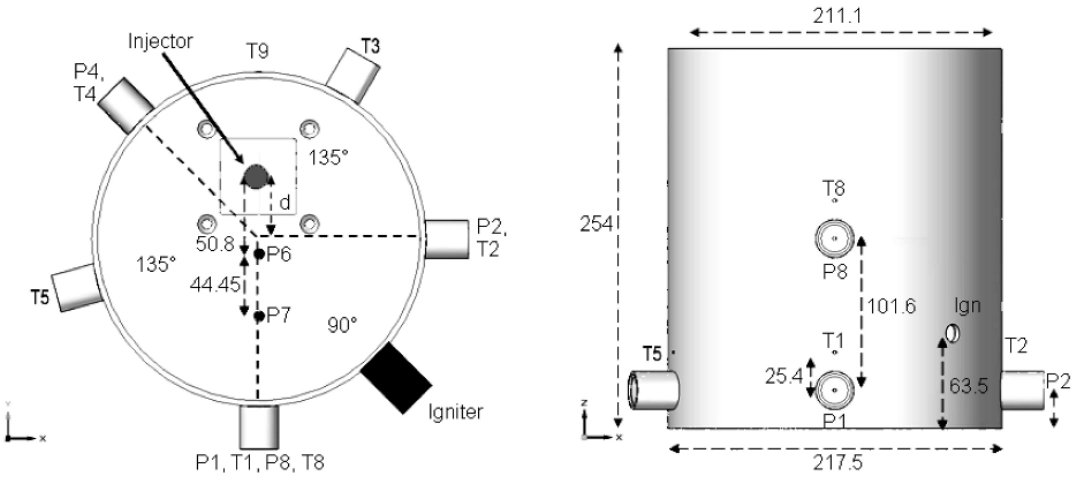

Figure 1.1: Atmospheric burner chamber

The chamber could be repositioned relative to the injector to excite the different modes of the chamber during operation. The acoustic environments that an injector may experience can be divided into four mode types: radial, tangential, longitudinal, and combined modes. These correspond to the natural acoustic modes of the cylindrical combustion chamber. Experiments [4] demonstrated that radial, tangential, and combined radial-tangential modes can be produced in single-injector tests with this setup. No strong longitudinal modes were seen with the open-ended chamber. Their absence was likely due to lacking a chamber exit restriction to reflect pressure waves. Only radial modes showed significant presence in the chamber-centered cases in experimental studies that used a shear-coaxial injector [9].

The injector used in the shear-coaxial tests was based on a Rocketdyne injector, which was chosen because test data from full-scale, multiple-injector engine experiments were available [10]. Comparing the data from this single-injector experiment with the multiple-injector experiment will aid in future design and qualification

work to better understand scaling between smaller rocket tests to full-size rocket engines. This experimental methodology served as the basis for the CFD methodology described in the present study.

Sozer et al. [11] compared experimental results to numerous studies that used Loci-CHEM to model chamber wall heat flux in a long thin combustion chamber capped with a choking nozzle. The experiments and CFD studies used a shear-coaxial, gaseous oxygen/hydrogen rocket injector. Lian and Merkle [12] modeled that combustor experiment using a Reynolds-averaged-Navier-Stokes model (RANS) and a blended RANS/"Detached-Eddy-Simulation-like" (DES-like), two-dimensional scheme. They found that time averaging the solution from the "DES-like" simulation resulted in markedly better agreement with experimental wall heat flux data than the steady-state RANS simulations did. Smith [13] conducted extensive work comparing CFD simulations with combustion instabilities experiments using that apparatus. Nusca [14] conducted preliminary CFD studies looking at injector-chamber coupling of HFCI based on oxygen/methane pentad injector experiments with the UAHuntsville PRC atmospheric chamber setup.

1.3 Combustion Instabilities

Combustion instabilities in LREs are generally classified by the frequency ranges in which they occur [2]. Low frequency (<400 Hz) CI usually stem from coupling with structural vibrations in the larger structure of the rocket. These are often referred to as "pogo" instabilities. Mid-range frequency CIs usually originate in pumps, piping, and the other propellant delivery devices of the LRE. High-frequency

CI (>1000 Hz), also known as "screeching" or "screaming" instabilities, are usually associated with the coupling with thrust chamber acoustics.

Capturing HFCI was the focus of the current work. As stated earlier, this is the most potentially destructive form of CI. Designing baffles or resonators into a LRE thrust chamber is sometimes used to shift or dampen some resonant acoustic frequencies of the chamber away from frequencies excited during experiments conducted in the development process or those expected from previous experience.

To some degree, the resonant modes experienced during the operation of a chamber can be known ahead of time. For instance, for a roughly cylindrical chamber of radius R and length L filled with a gas having an average speed of sound a_{avg}, linear acoustic theory [15] predicts resonant modes at frequencies

$$f_{lmn} = \frac{a_{\text{avg}}}{2\pi}\sqrt{\left(\frac{j'_{mn}}{R}\right)^2 + \left(\frac{l\pi}{L}\right)^2}, \tag{1.1}$$

where l, m, and n are the integer mode numbers for the longitudinal, tangential, and radial directions, respectively, and j'_{mn} is the nth extremum of the mth Bessel function of the first kind. The a_{avg} may be found from the average chamber temperature and gas composition: $a_{\text{avg}} = \sqrt{\gamma_{\text{avg}} R_u T_{\text{avg}}/\mathcal{M}_{\text{avg}}}$. These modes may be classified by the direction in which the acoustic fluctuations take place: radial, tangential, and longitudinal. At some modes, resonant fluctuations can occur in multiple directions. As shorthand, the various natural modes may be referenced with a letter-number combination. For example, R1, T2, and L1R2 would identify the first radial mode,

the second tangential modes, and the first longitudinal, second radial combined mode, respectively.

1.4 Problem Description

The aim of this research was to develop a CFD methodology for the analysis of atmospheric-burner tests conducted at the UAHuntsville PRC. This thesis served as the first step to that end. The initial test case used a shear-coaxial injector based on the Rocketdyne design (Figure 1.2). The atmospheric burner tests used gaseous methane and gaseous oxygen propellants [9]. In the experiments, the full-size rocket injector was mounted flush with the top of the test stand. A chamber instrumented with pressure transducers and thermocouples was positioned atop the test stand as shown in Figure 1.1 such that the center of the injector was a specified distance from the chamber wall.

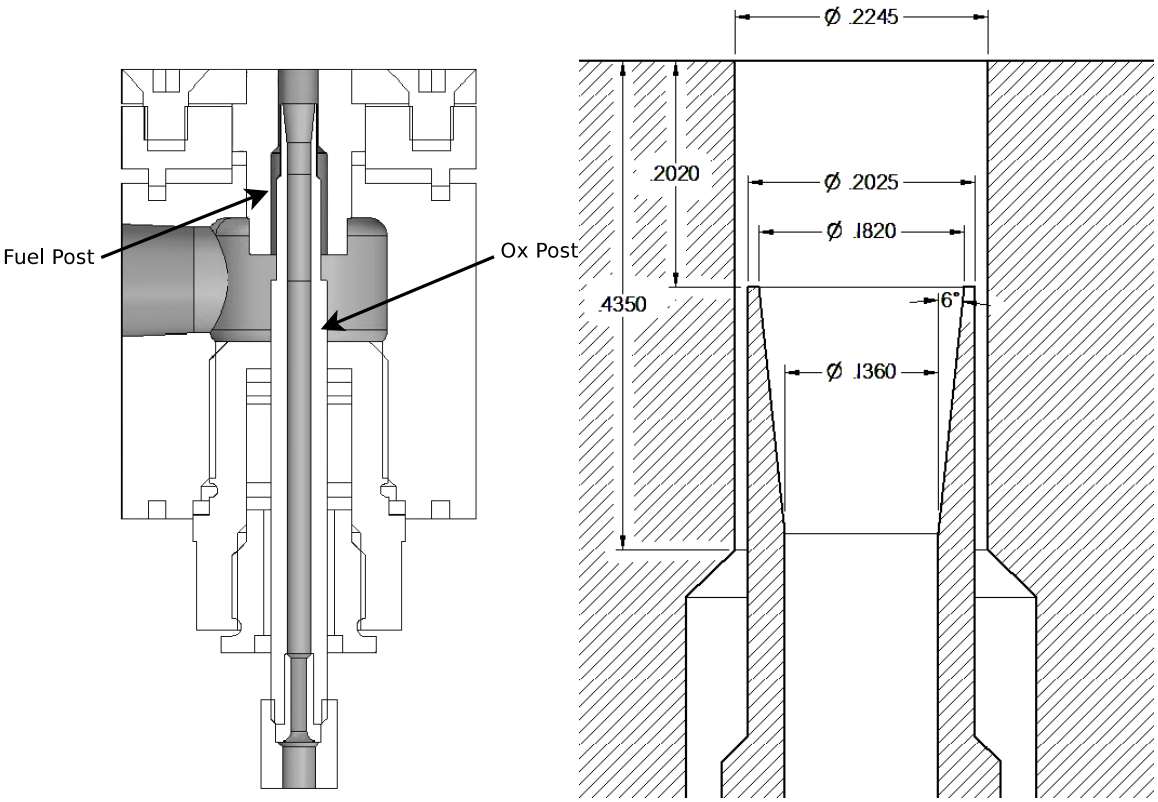

(a) experimental assembly (b) injector dimensions

Figure 1.2: Rocketdyne injector

CHAPTER 2

MATHEMATICAL MODELING AND METHOD OF SOLUTION

There is nothing more practical
than a good theory.

—L. Boltzmann

2.1 Governing Equations

Compressible, variable-property, reacting, Newtonian flow is governed by the Navier-Stokes equations [16]:

$$\frac{\partial \tilde{U}}{\partial t} + \frac{\partial \tilde{F}_i}{\partial x_i} + \frac{\partial \tilde{D}_i}{\partial x_i} = \tilde{S} \tag{2.1}$$

where

$$\widetilde{U} = \begin{bmatrix} \rho_s \\ \rho v_j \\ \rho E \end{bmatrix}, \tag{2.2a}$$

$$\widetilde{F}_i = \begin{bmatrix} \rho_s v_i \\ \rho v_i v_j + p\delta_{ij} \\ v_i \left(\rho E + p\right) \end{bmatrix}, \tag{2.2b}$$

$$\widetilde{D}_i = \begin{bmatrix} \rho_s V_{si} \\ -\tau_{ij} \\ -\tau_{ij} v_j - q_i + \sum h_s \rho_s V_{si} \end{bmatrix}, \tag{2.2c}$$

$$\widetilde{S} = \begin{bmatrix} \dot{w}_s \\ 0 \\ 0 \end{bmatrix}, \tag{2.2d}$$

with the stress tensor

$$\tau_{ij} = \mu \left(\frac{\partial v_i}{\partial x_j} + \frac{\partial v_j}{\partial x_i} - \frac{2}{3} \frac{\partial v_k}{\partial x_k} \delta_{ij} \right), \tag{2.3}$$

and total energy E being the sum of kinetic energy and internal energy:

$$E = \frac{1}{2} v_i v_i + E_{\text{internal}}. \tag{2.4}$$

The internal energy includes the energy of formation of each species as they are converted.

Species diffusion is handled in the diffusion flux term (2.2c) through the diffusion velocity and is governed by Fick's law:

$$\rho_s V_{si} = -\rho D_s \frac{\partial Y_s}{\partial x_i}. \tag{2.5}$$

Chemical reactions are handled in the source term (2.2d) through the production rate $\dot{w}_s$. For reactions of the form

$$\sum_s^{NS} \nu'_{s,r} X_s \underset{k_{b,r}}{\overset{k_{f,r}}{\rightleftharpoons}} \sum_s^{NS} \nu''_{s,r} X_s, \tag{2.6}$$

the production rate of species s is

$$\begin{aligned}\dot{w}_s &= \frac{\partial \rho_s}{\partial t} \\ &= \mathcal{M}_s \sum_{r}^{NR} \left(\nu''_{s,r} - \nu'_{s,r}\right) \left[k_{f,r} \prod_{l}^{NS} \left(\frac{\rho_l}{\mathcal{M}_l}\right)^{\nu'_{s,r}} - k_{b,r} \prod_{l}^{NS} \left(\frac{\rho_l}{\mathcal{M}_l}\right)^{\nu''_{s,r}}\right].\end{aligned} \tag{2.7}$$

2.2 Finite-Volume Method

Loci-CHEM [17] uses the Finite-Volume Method (FVM) to discretize the governing equations (2.1). Writing these equations in integral form for an individual cell c yields domain terms and surface terms:

$$\frac{d}{dt}\int_{\Omega_c} \tilde{U} d\Omega + \int_{\Gamma_c} \left(\tilde{F}_i + \tilde{D}_i\right) \cdot n_i d\Gamma = \int_{\Omega_c} \tilde{S} d\Omega. \tag{2.8}$$

Loci-CHEM uses a cell-centered form where properties over the cells are approximated as those at the cell center,

$$\int_{\Omega_c} \left(\frac{d}{dt}\tilde{U}(\tilde{x},t) - \tilde{S}(\tilde{x},t)\right) d\Omega \approx \left(\frac{d}{dt}\tilde{U}_c(t) - \tilde{S}_c(t)\right) \Omega_c, \tag{2.9}$$

and the surface fluxes are approximated with the face-midpoint value,

$$\begin{aligned}\int_{\Gamma_c} \left(\tilde{F}_i(\tilde{x},t) + \tilde{D}_i(\tilde{x},t)\right) \cdot n_i d\Gamma &= \sum_{f}^{NF_c} \int_{\Gamma_{c,f}} \left(\tilde{F}_i(\tilde{x},t) + \tilde{D}_i(\tilde{x},t)\right) \cdot n_i d\Gamma \\ &\approx \sum_{f}^{NF_c} \left(\tilde{F}_f(t) + \tilde{D}_f(t)\right) \Gamma_{c,f},\end{aligned} \tag{2.10}$$

where $\tilde{F}_f$ and $\tilde{D}_f$ are the normal fluxes at the midpoint of surface f of the cell.

Thus, (2.1) may be approximated locally in the cell-centered FVM as

$$\Omega_c \frac{d}{dt}\tilde{U}_c(t) = -\sum_{f}^{NF_c} \left(\tilde{F}_f(t) + \tilde{D}_f(t)\right) \Gamma_{c,f} + \tilde{S}_c(t)\Omega_c. \tag{2.11}$$

Loci-CHEM solves this ordinary differential equation in time using a Beam and Warming time integration scheme. Within the Newton iterations of the time steps, the spatial system of equations is solved by linear solvers implemented in Loci-CHEM. Greater detail of how Loci-CHEM implements these methods and how it handles the flux terms and turbulence made be found in its documentation [17].

2.3 CFD Tools

The CFD package used for the current work was Loci-CHEM developed by Luke, et al. [17] at Mississippi State University. Loci-CHEM uses the finite-volume method on unstructured meshes to solve the Navier-Stokes, chemically-reacting-flow equations (2.1). The experimental geometry was draw in wireframe form using a software package called SolidMesh [18] where it was prepared for mesh generation. SolidMesh has an internal interface to an unstructured grid program called AFLR [19]. The AFLR program used an advancing-front/local-reconnection method to generate unstructured grids for the boundary surfaces and domain volumes to be used in the CFD computations. Both SolidMesh and AFLR were also developed at Mississippi State University.

2.4 CFD Procedure

In the interior of the chamber where burning occurs, it was recommended to have several grid points per flame thickness to capture the combustion chemistry. Grid points were also concentrated around the shear/mixing layer in the injector recess to better capture the turbulence and mixing that is crucial to the overall system behavior. The flame thickness for a laminar methane flame is approximately 0.1 mm. Larger flame thicknesses were observed during earlier Bunsen burner tests (Section 3.1.3.2). In regions expected to experience combustion, the grid spacing ranged from about 0.04 mm to 0.1 mm (Figure 2.1 (c)). Further grid refinement did not change the observed flame thickness in the Bunsen burner tests.

In addition to capturing combustion chemistry, fluctuating acoustic phenomena also needed to be preserved as they propagate through the domain. Using the method of manufactured solutions (MMS), Roy et al. [20] have shown Loci-CHEM to be between first- and second-order accurate. Therefore, a maximum grid element size was estimated such that 1.5-order accuracy could be maintained for unsteady phenomena throughout the computational domain. Based on a curvefit of Tam and Webb's analysis [21] of standard finite-difference schemes of second-, fourth-, and sixth-order accuracy in the first derivative, a 1.5-order spatially accurate scheme would require at least 22 points per wavelength to preserve a given frequency. The spatial resolution used was estimated to maintain frequencies up to 6000 Hz without attenuation. This estimate was based on the speed of sound in air at atmospheric pressure and room

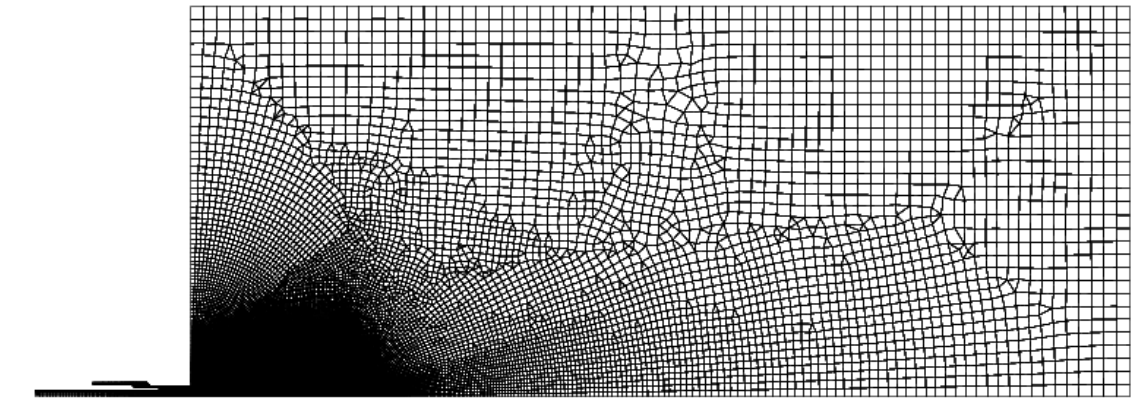

(a) Experimental domain

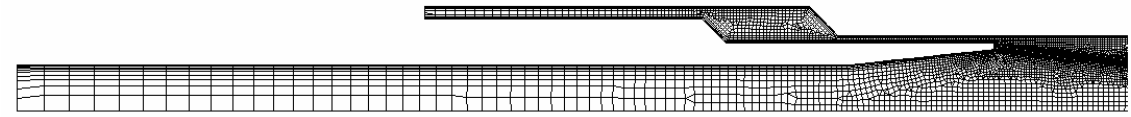

(b) Injector entry

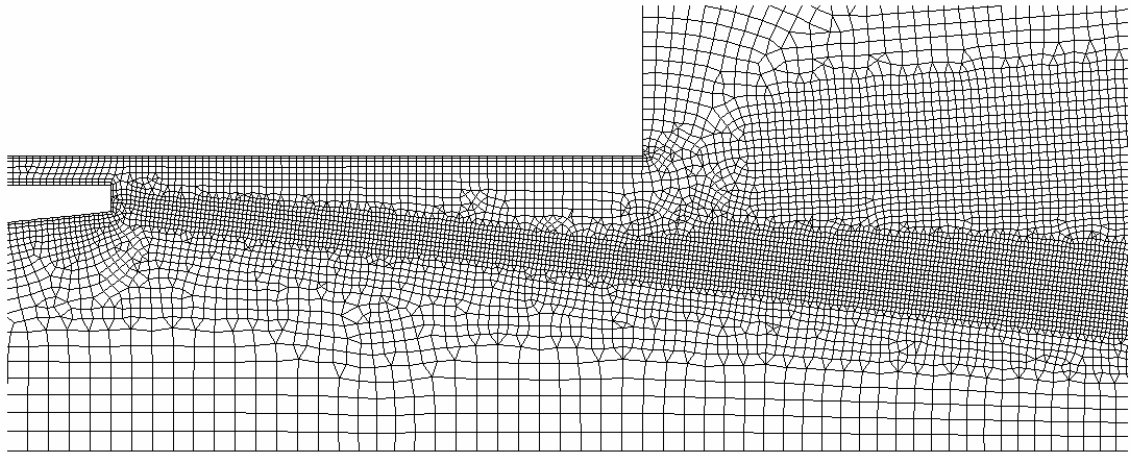

(c) Mixing region near the injector exit

Figure 2.1: Computational Domain

temperature (a $\approx$ 346 m/s). Since the average chamber temperature would be above room temperature, node spacings were deemed to likely be sufficient.

Half the domain was gridded (Figure 2.1 (a)) and then extruded in a one-degree slice to make a three-dimensional, axisymmetric grid. Modeling the experiment as axisymmetric will lose any tangential modes; however, for the chamber-centered case

that was run in this study, these modes did not have a strong presence during the experiments [9].

Initial cold-flow simulations were run on a coarser mesh to have turbulent mixing and the shear region setup before mixture ignition. This cold-flow solution was then used to initialize a simulation on a grid with better resolution in areas near the injector where reactions would occur. The experiment setup used an H2/O2 igniter to light the burner (see Figure 1.1). To simulate this, a 4 mm wide column of hot steam was superimposed on the cold-flow solution at 8 mm from the fireface to initiate ignition. Along the length of the steam column, the peak temperature and the peak steam concentration were set to 2200 K and 100 percent, respectively. Across the the width of the column, temperature and hydrogen concentration were given a Gaussian distribution that decreased to the cold-flow solution levels. During the process of flame propagation, the time-step of the simulation was reduced about an order of magnitude to capture the physics of the problem. After this initial flame propagation through much of the reactable mixture, the time-step was relaxed back to 2.0×10^{-7} seconds.

2.5 Turbulence Modeling

The problem at hand was highly unsteady and turbulent; therefore, the hybrid RANS/Large Eddy Simulation (RANS/LES) option available with Loci-CHEM was used. The LES sub-grid-scale modeling portion of the hybrid scheme allows more turbulent structures to be captured than if only a RANS model was used. These smaller structures contribute to exciting other high frequency fluctuations in the flow such as

in chemical composition. For two-dimensional and axisymmetric cases, Loci-CHEM has an option to use an LES formulation that ignores the third dimension. Several RANS models were available in Loci-CHEM. The Menter's Shear-Stress Transport (SST) option was chosen as the RANS model portion of the hybrid scheme for the current study. The SST model incorporates the transport of the turbulent shear stress into the eddy viscosity in Mentor's baseline model (BSL) which uses a k-ω model close to the wall and a k-ϵ far from the wall [17].

Roy et al. [20] has shown by MMS that Loci-CHEM's implementation of Menter's baseline turbulence model, on which the SST is based, to be about second-order accurate with a mesh made of exclusively Cartesian quadrilateral elements and about first-order accurate when an unstructured mesh made up of triangular elements was used. The grid for this injector study used mostly quadrilateral-based elements with minimum triangular elements.

CHAPTER 3

RESULTS AND DISCUSSION

3.1 Benchmark Problems

Loci-CHEM's ability to handle the physical phenomena important to the experiment needed to be established before proceeding to more complicated simulations. As discussed in Chapter 1, the three main phenomena effecting combustion instability are chemistry, acoustics, and turbulence. As stated in Section 2.5, Menter's baseline turbulence model in Loci-CHEM had already been characterized by MMS and was thus not tested independently in the following benchmarking studies. In this section, the finite-volume-based Loci-CHEM shocktube (Section 3.1.1) and acoustics (Section 3.1.2) results will be compared with Tashakkor's [22] results from the Discontinuous-Galerkin-based (DG) code Loci-THRUST.

3.1.1 Shocktube

The shocktube problem serves as a standard problem for seeing how well a code can capture discontinuities and strong gradients in flow properties. Strong gradients are present in flames, so Loci-CHEM's ability to handle strong gradients needed to be tested.

Table 3.1: Shock tube initial conditions

Section	Pressure (kPa)	Temperature (K)
Driver	150	250
Driven	50	350

The shocktube problem was set up with air using the conditions in Table 3.1 across the initial contact at $x = 0$. With the help of built-in Barth limiter, Loci-CHEM was able to capture the discontinuities of the flow without any noticeable oscillations around the disconituities and little dissipation (Figure 3.1). The CFD results agreed very well with the analytic solution.

3.1.2 Acoustics

Loci-CHEM's ability to handle acoustics was not known prior to beginning the current work. The benchmarking problems used in this study were based on those used by Tashakkor [22] which were based in part those of Tam and Webb [21].

3.1.2.1 Acoustic Pulse

A two-cell thick, square domain was initialized with standard sea-level conditions then superimposed with a 1 percent, Gaussian pressure disturbance. This resulted in a circular pressure wave propagating toward the boundaries. Figure 3.2 shows the progression of the pressure pulse for various grid resolutions compared with the exact solution. As expected, denser grids appeared to converge to the exact solu-

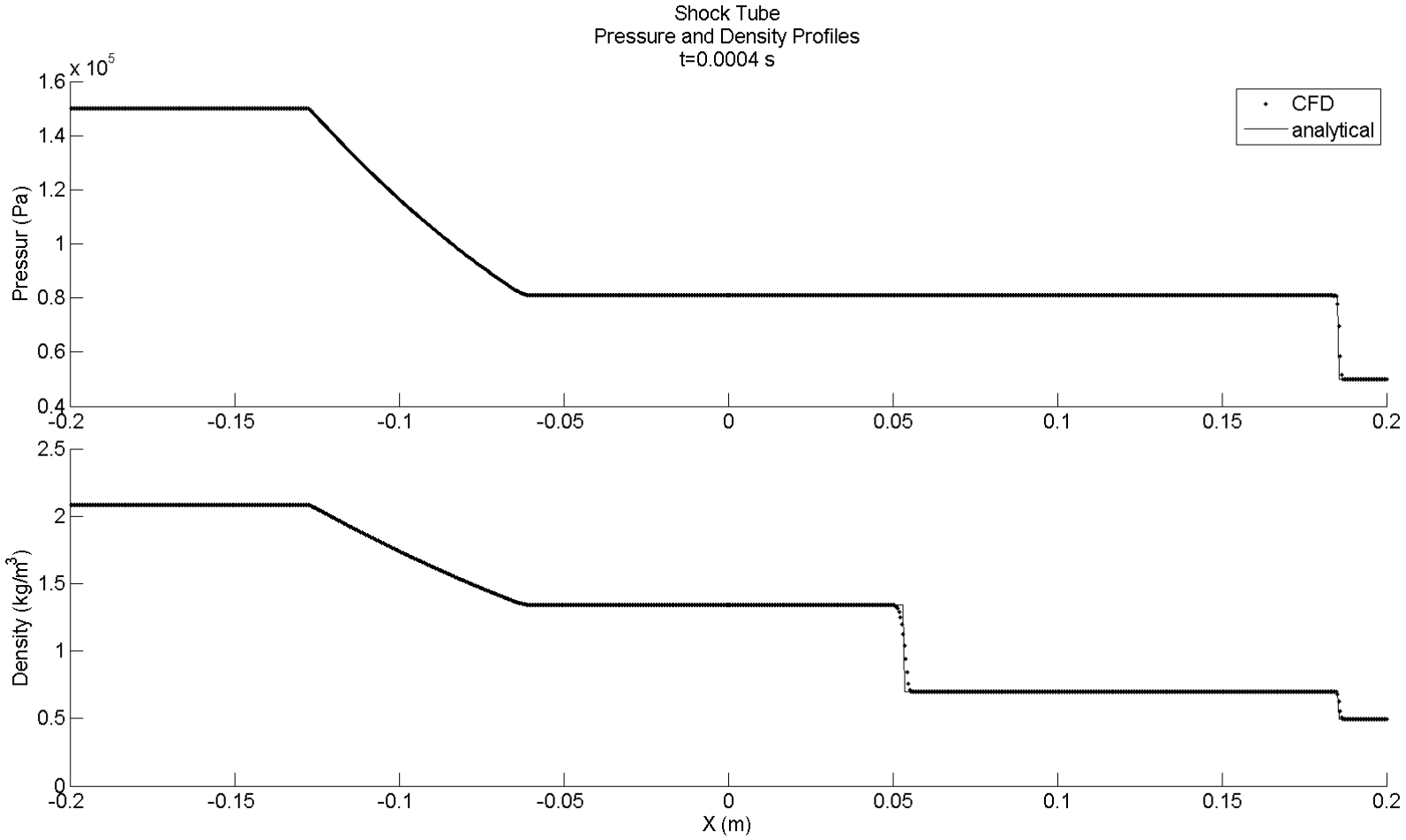

Figure 3.1: Air shocktube CFD results and analytic solution

tion. Compared with Tashakkor's [22] DG results, Loci-CHEM required very dense grids to capture the wave (Figure 3.2).

3.1.2.2 Chamber Frequencies

Loci-CHEM's ability to capture the natural acoustic modes of a chamber was also tested. This used a two-dimensional chamber the natural frequencies of which may be calculated from [15]

$$f_{nm} = \frac{a}{2}\sqrt{\left(\frac{n}{L_x}\right)^2 + \left(\frac{m}{L_y}\right)^2} \qquad n, m = 0, 1, 2, \ldots \tag{3.1}$$

where f_{nm} is the natural frequency of the (n,m) mode, a is the speed of sound, and L_x and L_y are the chamber length and width, respectively. A 6 cm by 6 cm chamber on a 41 by 41 grid filled with air at atmospheric pressure and 1220 K was initialized with four randomly positioned Gaussian 20-percent-over-pressure disturbances with 2.25 mm radius half-widths. The walls of the chamber were given reflecting boundary conditions, and the out-of-plane boundaries were set symmetric boundary conditions. Several pressure probes were placed near the reflecting boundary (Figure 3.3). The pressure time signal for probe location 1 is shown in Figure 3.4. The natural frequencies of this chamber found from Equation 3.1 are shown in Table 3.2.

To determine the frequencies excited in chamber by the pressure disturbances, a Fast Fourier Transform (FFT) was applied to the time history of the pressure signals at the probed locations. Figure 3.5 shows the spectral energy density of the signals from two of these probes. It should be noted that the highest frequency mode

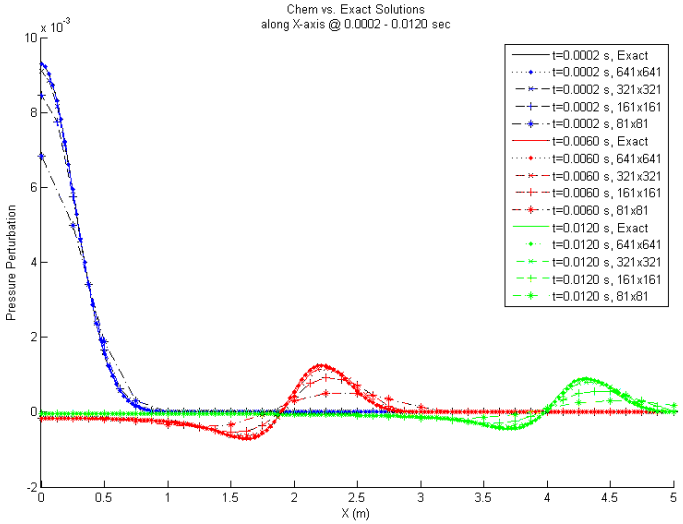

(a)

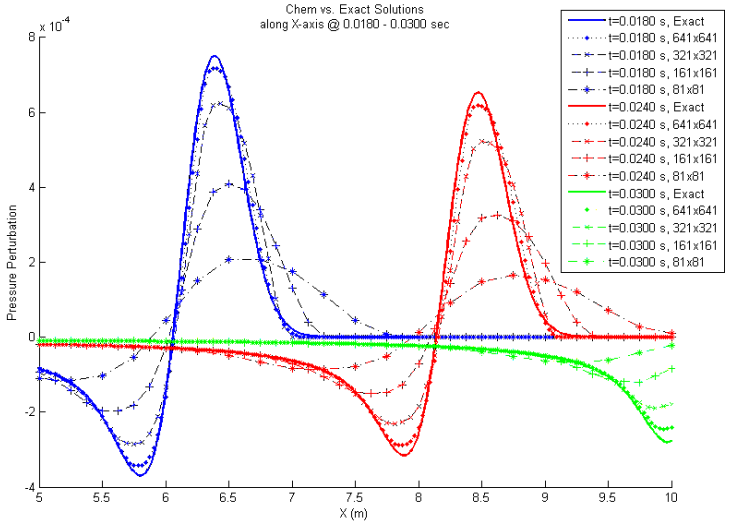

(b)

Figure 3.2: Pressure distribution through time

Table 3.2: Natural acoustic modes of a 6 cm by 6 cm chamber with air

n\m	0	1	2	3	4
0	0.0	5.847	11.693	17.540	23.387
1	5.847	8.268	13.074	18.489	24.107
2	11.693	13.074	16.537	21.081	26.147
3	17.540	18.489	21.081	24.805	29.234
4	23.387	24.107	26.147	29.234	33.074
	kHz	kHz	kHz	kHz	kHz

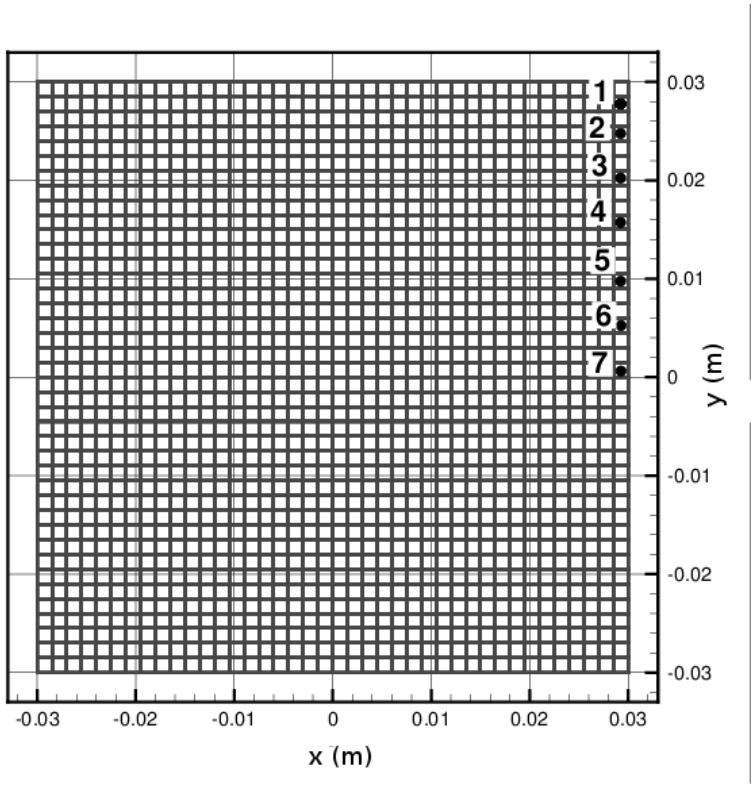

Figure 3.3: 6 cm by 6 cm chamber grid and probe locations

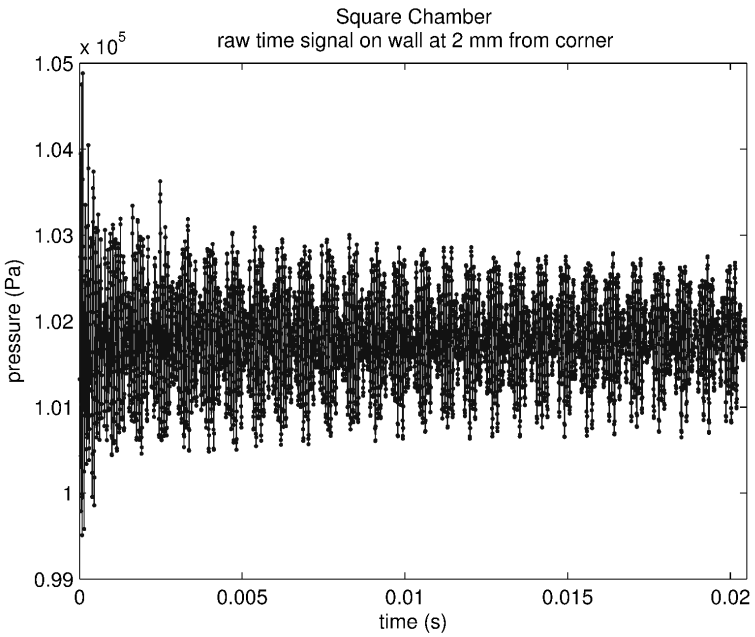

(a) Signal

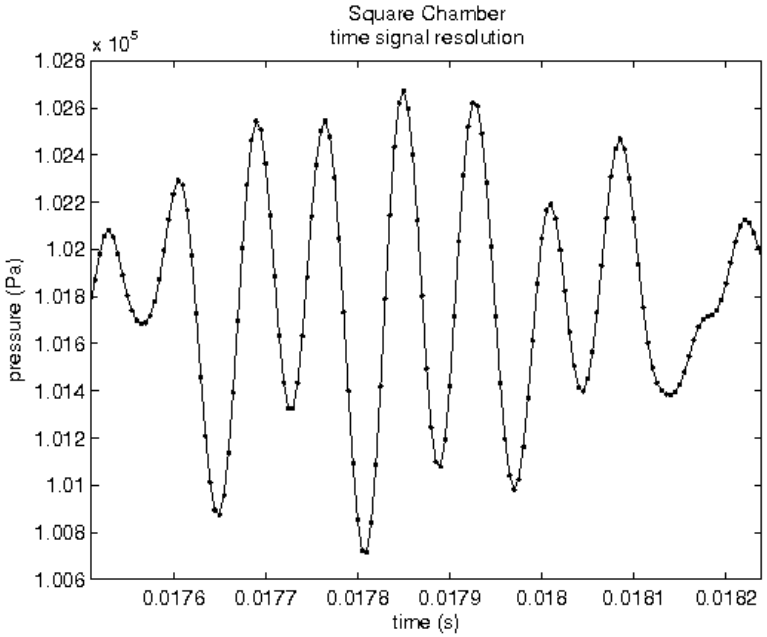

(b) Resolution of signal

Figure 3.4: Pressure signal on wall 2 mm from corner in 6 cm by 6 cm square chamber

Table 3.3: Comparison of analytical modes and CFD frequency peaks of a 6 cm by 6 cm chamber

mode	(0,1)	(1,1)	(0,2)	(1,2)	(2,2)	(0,3)	(1,3)	-	(2,3)
Analytic	5.847	8.268	11.693	13.074	16.537	17.540	18.489	-	21.081
CFD	5.857 kHz	8.248 kHz	11.71 kHz	13.08 kHz	16.54 kHz	17.57 kHz	18.55 kHz	18.94 kHz	21.13 kHz

that seems to have been preserved is 21 kHz (2,3), which corresponds to about a 22 points-per-wavelength spacing. This served to confirm the grid spacing estimates for preserving frequencies (Section 2.4). For the higher frequencies, peaks appeared at slightly higher frequencies than the nearest calculated mode frequency. This suggested that these modes were being excited, but the grid resolution was not sufficient to preserve them unaltered. Probe 4 at the one-quarter position on the chamber wall failed to capture the (2,2) mode. Additionally, all probes had a frequency peak at about 18.94 kHz which was just past the (1,3) mode. This frequency did not correspond to any natural modes of the chamber or their harmonics.

Tashakkor [22] captured all the natural frequencies of a square chamber up to at least the corresponding (3,3) mode using Loci-THRUST. Sadly no comparison could be drawn between the DG results and the current results from Loci-CHEM since the grid spacing, time properties, and shape function order used in obtaining the DG results could not be found in the source.

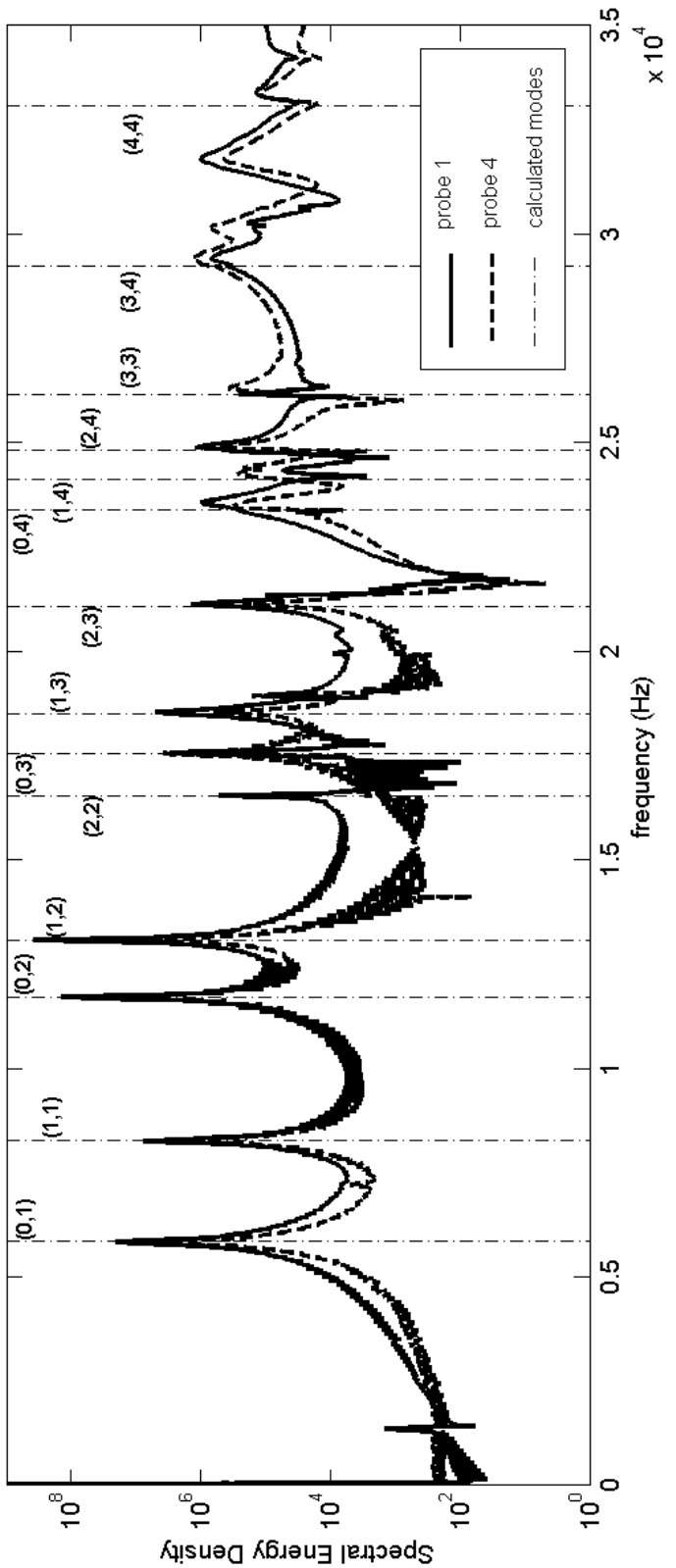

Figure 3.5: FFT of Pressure in 6 cm by 6 cm Square Chamber

3.1.3 Combustion

Since a new reaction to model methane/air combustion was being implemented in Loci-CHEM, this had to be tested as well. For the current study, nitrogen was treated as an inert species, and the methane combustion was modeled as complete combustion with oxygen through a one-step, global reaction.

$$CH_4 + 2O_2 \rightarrow CO_2 + 2H_2O \tag{3.2}$$

3.1.3.1 Combustion Model

The finite-rate chemistry model used in this study was based on a one-step, global reaction Arrhenius curvefit for methane-oxygen [1].

$$k_r = A_r T^{\eta} \exp(-E_a/R_u T) \tag{3.3}$$

where k_r is the reaction rate, T is the mixture temperature, and R_u is the universal gas constant. The parameters A_r (often referred to as the pre-exponential or frequency factor), E_a (the activation energy), and η are empirical constants. The reaction rate arises from finite-rate chemistry equations and species production terms. These constants vary with mixture ratio, but this study used the parameter values found for a stoichiometric mixture (Table 3.4) since the mixtures will range above and below stoichiometric. The parameters had been derived by curve fitting k_r from Equation 3.3 using an E_a and a modified A_r to a modified heat release equation for the detailed

Table 3.4: Coefficients for a one-equation methane/air reaction mechanism for a stoichiometric mixture, adapted from [1]

	Value	units
A_r	1.0342×10^{15}	$\mathrm{m^6\,kmol^{-2}\,s^{-1}}$
η	0.0	-
E_a	12175	$\mathrm{kJ\,kmol^{-1}}$
R_u	8.31434	$\mathrm{kJ\,kmol^{-1}\,K^{-1}}$
Q	47509	$\mathrm{kJ\,kg^{-1}}$
M_F	16.043	$\mathrm{kg\,kmol^{-1}}$
M_{Ox}	31.999	$\mathrm{kg\,kmol^{-1}}$
ν_F	1	-
ν_{Ox}	2	-

reaction mechanism [1].

$$q = QM_F\nu_F \left(\frac{\rho Y_F}{\mathcal{M}_F}\right)^{\nu_F} \left(\frac{\rho Y_{Ox}}{\mathcal{M}_{Ox}}\right)^{\nu_{Ox}} k_r \tag{3.4}$$

An important point is that the heat release from one-reaction model only seems to match the detailed chemistry on a narrow temperature range. Outside of the 1000 K to 2000 K temperature range, the heat release is under-estimated below 1000 K and slightly over-estimated above 2000 K when using the one-reaction curve fit; however, it should also be noted that the flame speed from the one-equation model was within 5 percent of the detailed chemistry model.

3.1.3.2 Laminar Flame Speed

Validating that the chemistry model (Section 3.1.3.1) was implemented properly focused mainly on reproducing the expected laminar flame speed (s_l) from Coffee

et al. [1]. This was originally attempted by running simple one-dimensional cases like those of Saxena [23] and Hood [24], which followed the propagation of a flame in a premixed medium. To this end, a quasi-one-dimensional, one-element thick domain was initialized with a stoichiometric methane-oxygen mixture at room conditions. In order to ignite the mixture, a Gaussian temperature distribution was superimposed on the mixture in the center of its length. The peak temperature was chosen to be about 1000 K, and the width of the distribution specified such that the enthalpy rise met the minimum ignition energy requirements for the mixture [25]. A square-type initial temperature was also tried. Both of these conditions yielded widely varying results with the speed of flame propagation relative to the local fluid velocity being one or two orders of magnitude greater than the expected flame speed of 38.4 cm/s [1].

Though flame speed is sometimes measured directly from flame propagation, it may also be estimated from stabilized flames. Bunsen burner experiments conducted by Natarajan et al. [26] and Dong et al. [27] have shown that taking the ratio of outer surface area (A_{outer}) (as defined by flame luminosity) of a stabilized flame and the volumetric flowrate ($\dot{V}$) of the premixed stream (Equation 3.5) shows good agreement with other experimental methods of determining laminar flame speed.

$$s_l \approx \frac{\dot{V}}{A_{\text{outer}}} \tag{3.5}$$

In the Loci-CHEM simulated flame, the outer flame surface was taken to be at the location of the highest gradient of heat release, based on the Equation 3.4, which was taken to roughly correspond to luminosity.

For benchmarking the newly implemented one-equation methane/air model from Table 3.4 in Loci-CHEM, a 2-mm-diameter tube was fed with a stoichiometric methane/air mixture at the equivalent of 7.29×10^{-5} kg/s with a total plenum temperature of 300 K. These conditions allowed a long flame to be created while remaining in the laminar flow regime. The outer flame surface was taken to be at the location of the highest gradient of heat release, as calculated from Equation 3.4, since heat release should be proportionate to flame brightness. These locations were fitted with a third-order curve from which an area of revolution was computed.

The laminar flame speed of approximately 52.5 cm/s was found, and the highest temperatures (Figure 3.6 (a)) computed were about 2310 K. The temperature was in excellent agreement with that measured by Coffee, Kotlar, and Miller [1] for their model; however, the flame speed was higher than theirs. The maximum heat release rate in Figure 3.6 (b) is above 7.60 kJ/m^{3}s, which was also higher than Coffee et al.'s. As stated above, heat release was used in this computation of outer flame surface area. It should be noted that heat release intensity may not correspond perfectly to visible spectrum emission. Thus, while there was some uncertainty in the flame speed determination, the results were deemed to be in sufficient agreement with those expected to move forward with injector modeling.

As stated in Section 2.4, tests of grid spacing in the flame region were conducted. These tests showed a flame thickness of approximately 6 mm. No thinning for the flame thickness was observed with grid spacings smaller than 0.04 mm.

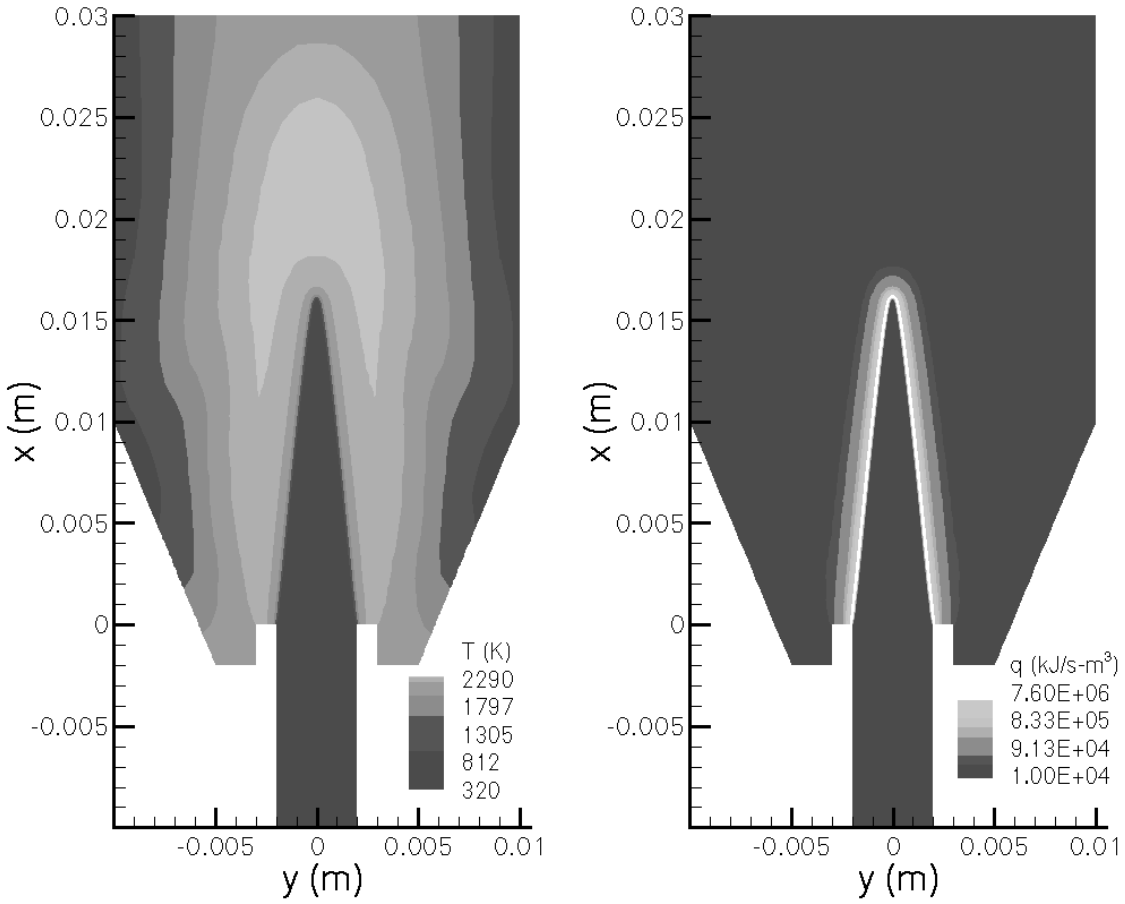

(a) Temperature

(b) Heat release

Figure 3.6: Bunsen flame temperature and heat release contours

3.2 Injector

After the performance of the one-equation methane-air model was quantified, work proceeded to modeling the injector combustion instability experiment described in Section 1.4. Figure 1.1 shows the geometry of the chamber and the location of the numbered pressure transducer locations which were used for comparing CFD results with the experimental data. CFD boundary conditions were based on UAHuntsville

Table 3.5: Experimental conditions and corresponding CFD boundary conditions

	Experiment	Loci-CHEM BC	Argument
Atmosphere	1 atm, 295 K	*not modeled*	
Top	open	farfield	p = 1 atm, T = 295 K, u = 0.0 m/s
Wall, Fireface, Ox Post, and Fuel Annulus	solid wall	viscousWall	adiabatic
Ox Supply	O_2: 0.654 g/s	fixedMass	mdot = 1.816667e-6 kg/s, T0 = 295 K, mixture=[O2=1.0]
Fuel Supply	CH_4: 0.352 g/s N_2: 0.951 g/s	fixedMass	mdot = 1.816667e-6 kg/s, T0 = 295 K, mixture=[CH4=0.27, N2=0.73]

PRC experimental test data (Table 3.5). It should be noted that the CFD mass flow rates represent a 1 degree slice of the injector flow.

3.2.1 Flowfield

Initial inspection of temperature contours (Figure 3.7) showed a flame attached at the lip of the oxidizer post. Within about 5 mm above the fireface, combustion took place in the shear layer between the central oxidizer stream and the fuel stream (Figure 3.7 (b)). Above 5 mm, the outer parts of the jet broke down into vortical structures, which encouraged mixing of the fuel stream, flame, and surrounding oxygen in the chamber. The strongest areas of heat release (Figure 3.8) were at the lip of the oxidizer post and in the vortical structures nearest the fireface. The reacting region of the flame was seen to extend about halfway up the chamber with a width of about 4 cm. As seen in Figure 3.8, a significant portion of the flame showed heat

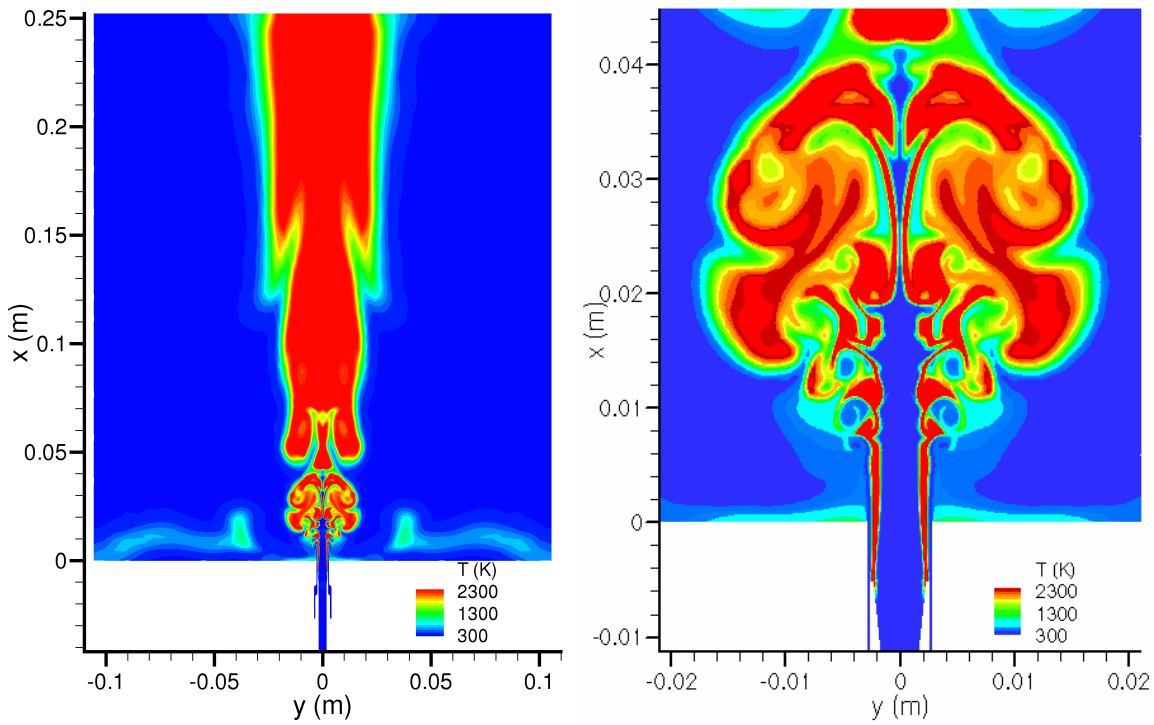

(a) Full domain

(b) Near-injector region

Figure 3.7: Temperature contours in atmospheric burner less than 2300 K

release greater than that found in the bunsen burner case. In fact, heat release values of over 318 kJ/m^{3}s were present in very thin regions in the flow.

In the near-injector region, a strong velocity difference existed between the fuel and oxidizer streams (Figure 3.9). The resulting shear flow served to encourage turbulent mixing of the propellants in the combustion zone. Downstream of the combustion zone, the flow should exhibit self-similarity. To show this the flowfield results from several time steps were averaged together. Figure 3.10 shows the averaged axial velocity profiles normalized to the peak of the profile at several locations between one-quarter of the chamber length and one-half the chamber length. The radial dimension was normalized by the radius where the velocity is half that of the peak.

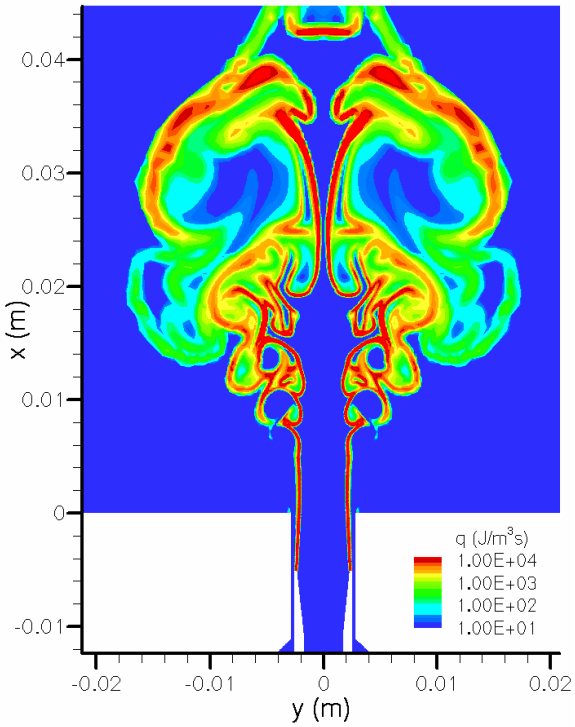

Figure 3.8: Heat release contours in atmospheric burner

This corresponded to 11 and 33 diameters downstream of the fireface. Outside this range the self similarity was not apparent. Upstream, the combustion zone was present, and downstream, Figure 3.11 (a) suggests that the flow may have been interacting with the exterior.

Figure 3.12 shows the mass fractions of the injected methane and the combustion products, respectively. Most of the methane had mixed with the injected oxygen or the chamber air or had been consumed within 1 cm of the fireface. Large vortical structures starting at about 5 mm aided strongly in the mixing. In the shear layer between the injected fuel and oxidizer streams showed strong production of combus-

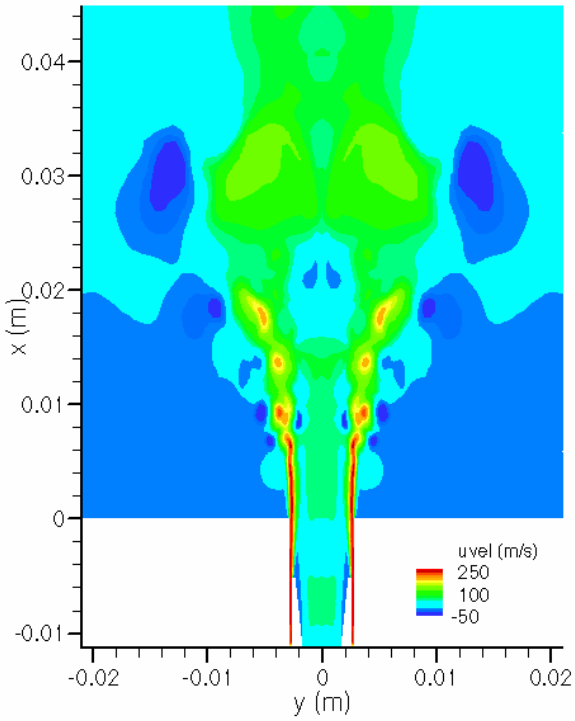

Figure 3.9: Axial velocity contours in atmospheric burner

tion products. Between 5 mm and 12 mm from the fire face, the region of vortical mixing nearest the first face showed large concentrations of products being produced.

3.2.2 Frequency Response

The pressure history for four pressure transducer locations (1, 6, 7, and 8) was captured using probes in the CFD analysis. Figure 3.13 shows a representative time history from probe location 1. Though the extrema appeared sharp, focusing on these points showed pressure fluctuations were captured very smoothly using a time step of 0.2 μs. The magnitude of pressure fluctuations were significantly different between the experimental results and the CFD results (Figure 3.14). For instance, the experimental transducer signal from location 1 had a consistent fluctuation of

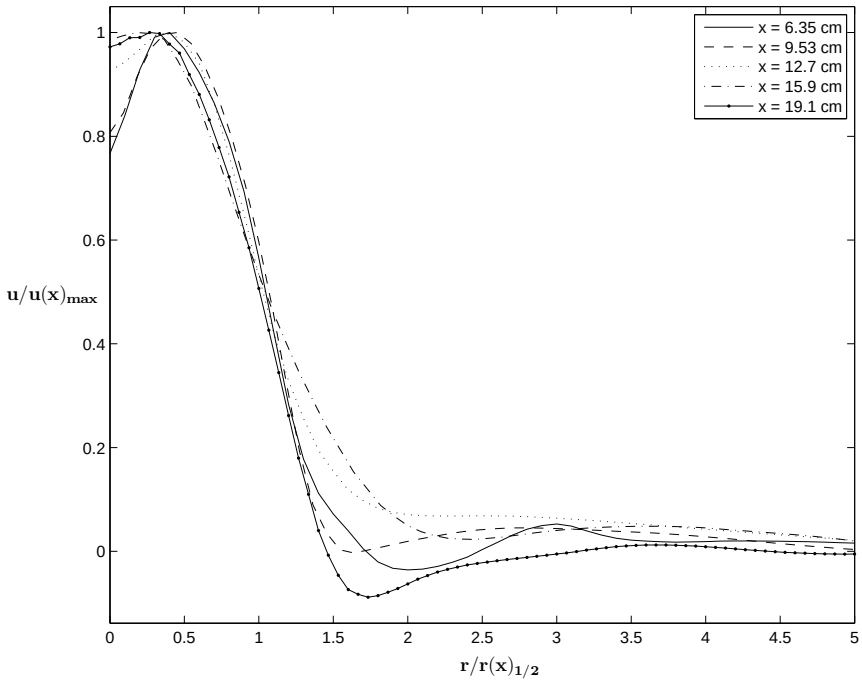

Figure 3.10: Axial velocity profiles

about 1.7 percent of the chamber pressure, while the CFD results from the same location showed a fluctuation of only about 0.5 percent of chamber pressure. Also, large amplitude, higher frequency instabilities appear in the experimental results periodically, which were not present in the CFD results. From Figure 3.15, it appears that the high amplitude, high frequency instability may, in fact, have been manifested in CFD analysis in the form of a small amplitude signal of the same frequency present throughout the pressure fluctuations rather than just appearing in short intervals.

As shown in Figure 3.16, analysis of the CFD results showed the strongest frequency to be around 2132 Hz. Figure 3.16 also shows a comparison between the CFD and the experimental results for the pressure fluctuation frequency response at

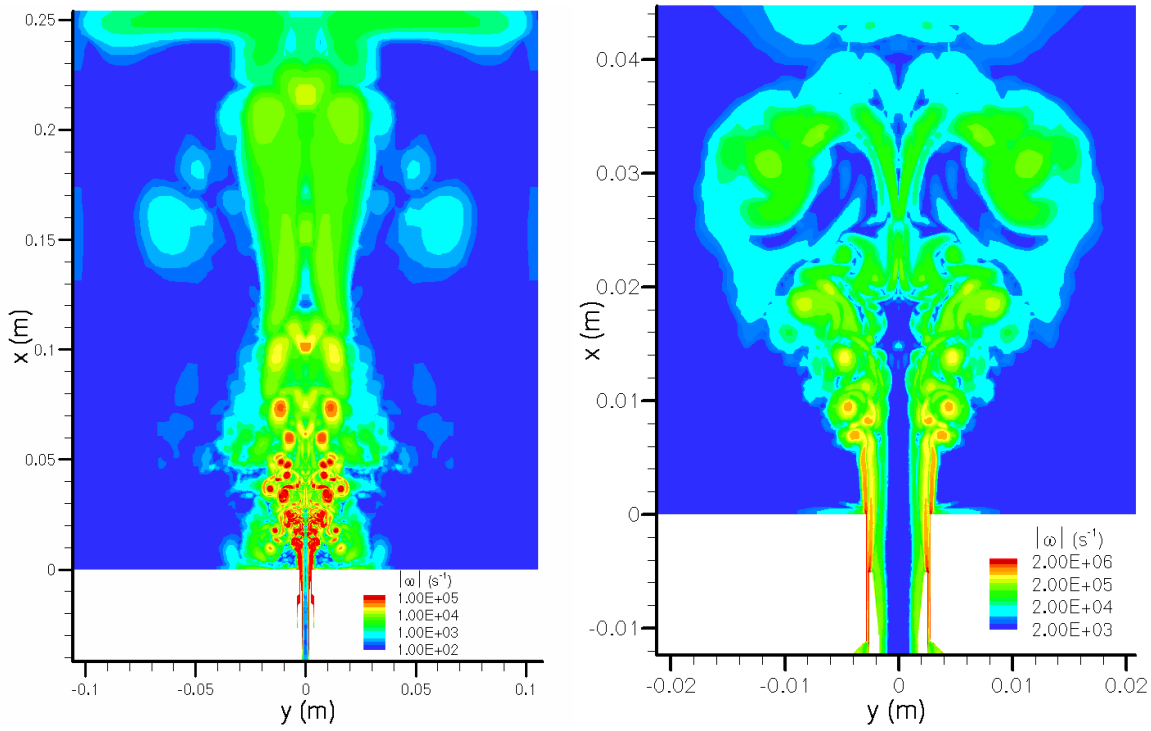

(a) Full domain (b) Near-injector region

Figure 3.11: Vorticity contours in atmospheric burner

transducer location 1; the dominant frequencies in the experimental responses were nearly identical at all probed locations in the axisymmetric chamber. This dominant frequency was seen in the pressure time history (Figure 3.14) as a persistent fluctuation. Though the dominant frequencies were very similar, the pressure fluctuations in the CFD results were much weaker. The periodic high frequency, high amplitude fluctuations seen in the experiment were at the edge of the Niquist frequency for the available signal. However, when the high amplitude portion of the signal was normalized to its peak amplitude and the CFD signal normalized to its peak amplitude (Figure 3.15), comparing locations of inflection points suggested that the high frequency may have also been present in the CFD analysis. To preserve the high

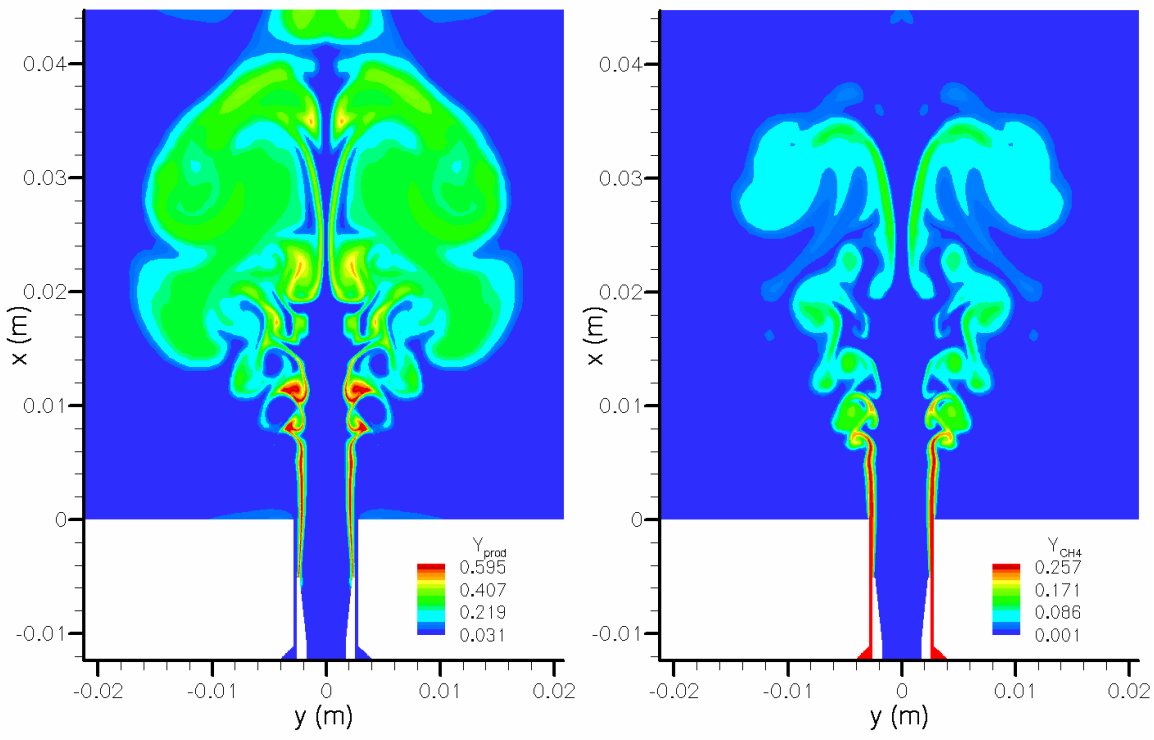

(a) Combustion products

(b) Methane

Figure 3.12: Species mass fractions in the near-injector region

frequency signal without attenuation and modification, the maximum grid spacing in the chamber would need to be decreased (see Section 3.1.2.2).

The negative shift in frequency was likely due to the average temperature in the chamber being cooler due to a lower chamber temperature in the CFD analysis than in the experimental chamber since the experiments were conducted in an open bay. During CFD setup, it was assumed that the chamber would warm up from room temperature. The average temperature of the chamber stayed near the initial and exit conditions. This may have also been the case for the experimental chamber with atmospheric gases being entrained into the chamber keeping the chamber temperature

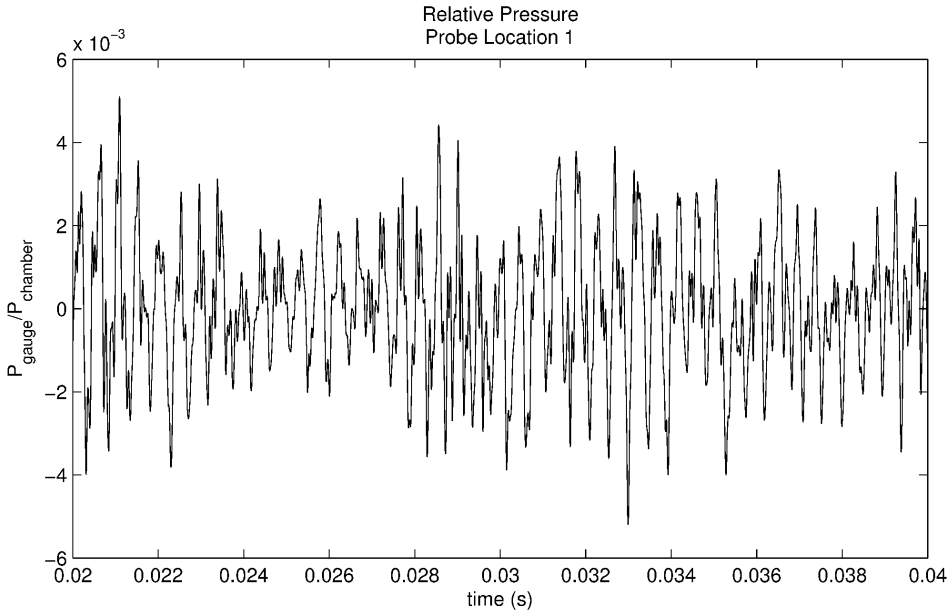

Figure 3.13: Relative pressure time history of CFD results from probe location 1

near the external conditions. A warm Alabama summer day could account for the elevated temperature in the experiment. Another possibility is that accumulated heating from long operation of the experimental apparatus may have raised the overall chamber temperature. The lower average temperature in the CFD analysis would have lowered the natural frequencies of the chamber since the speed of sound would be lower in the cooler chamber.

Since the relative magnitude difference between the experimental signals and the CFD are similar across all the transducer locations, the signal weakness is not likely due to poor grid resolution. Also, since the fuel and oxygen streams were allowed to develop from stagnation conditions, any upstream turbulence present in the experimental feed system would not be captured. Loci-CHEM's thickening of the flame region may also yield less powerful heat release leading to less powerful

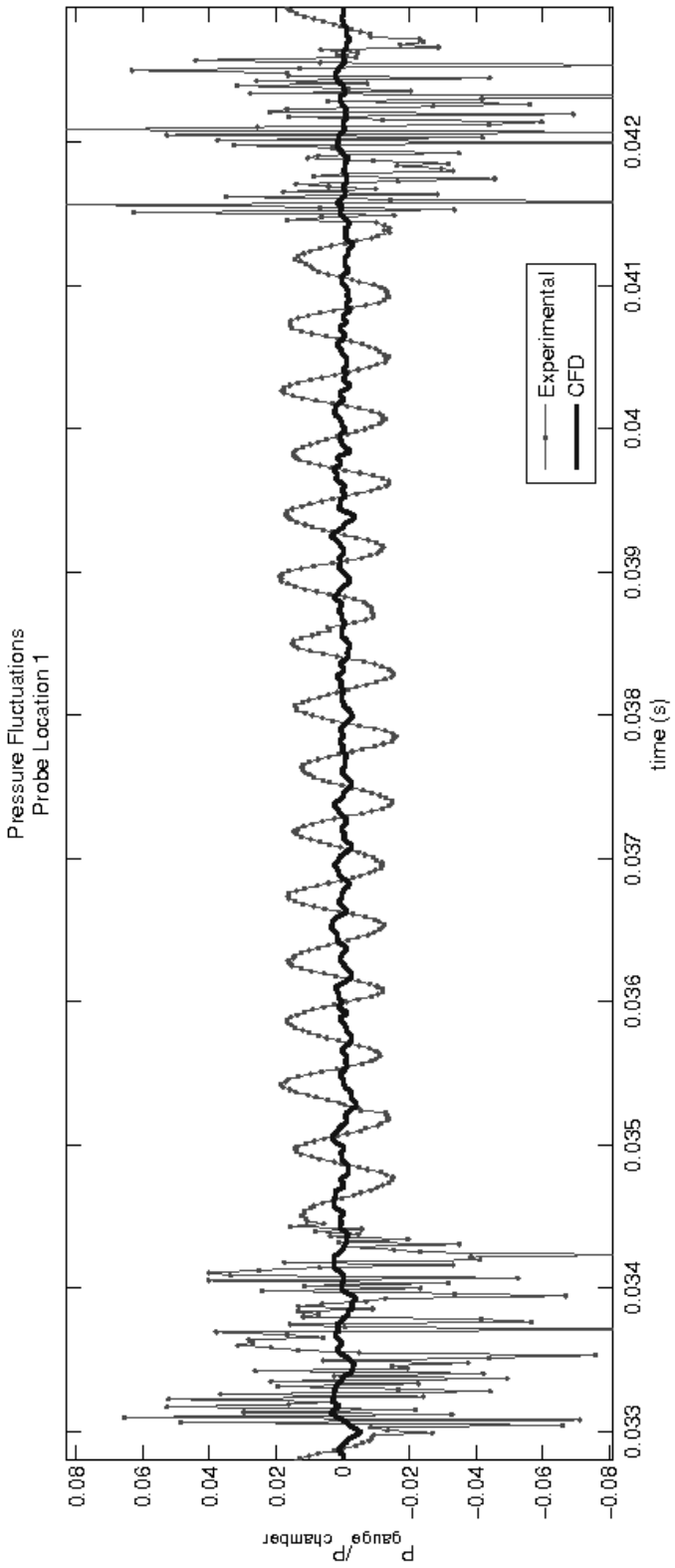

Figure 3.14: Pressure history comparison between experimental and CFD results

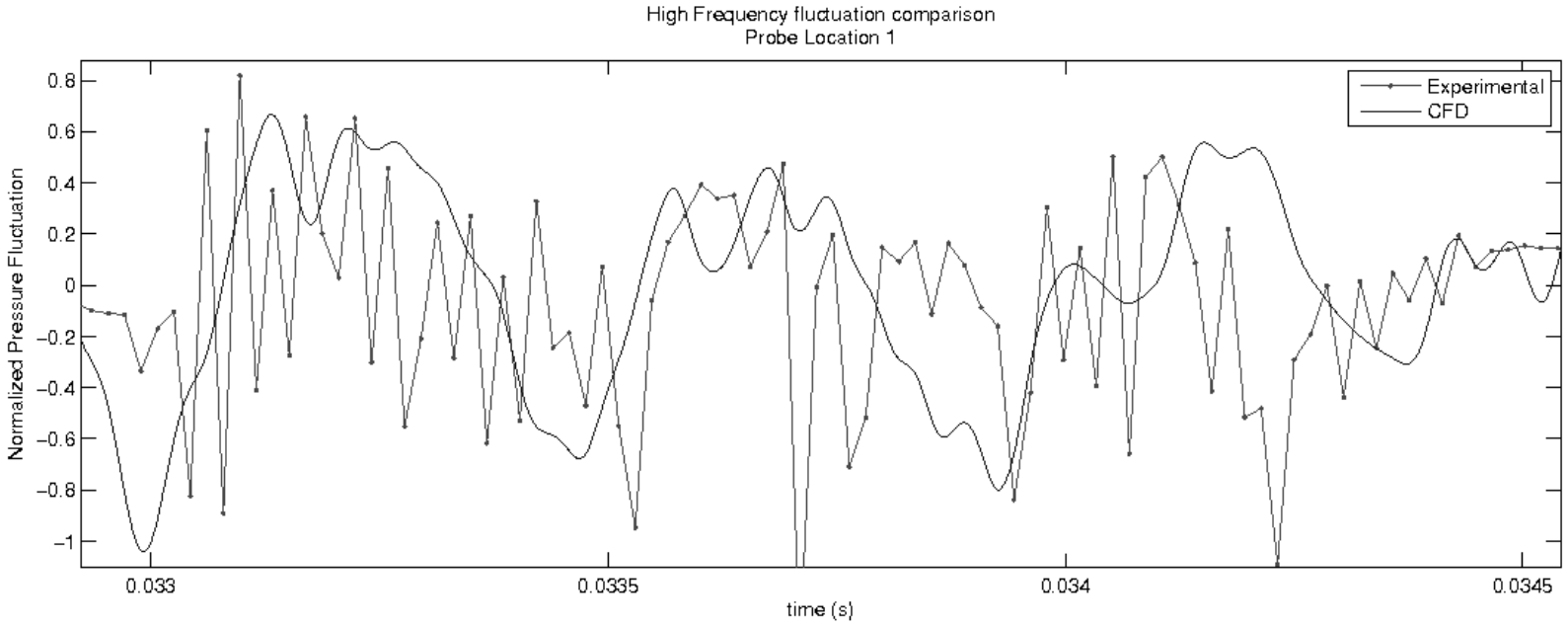

Figure 3.15: Pressure history comparison between experimental and CFD results normalized to high frequency instability amplitude

fluctuations. When this is coupled with the heat release and flame speed being higher than expected during the bunsen burner analysis in Section 3.1.3.2 these results are perplexing. There is also a possibility that the out-of-plane turbulent structures make important contributions to the strength of fluctuations. Since the experiment was modeled in an axisymmetric configuration, any of these effects would be lost.

The rest of the spectrum showed a weak, broad-band noise response that fell off around 10 kHz for location 8 persisted to higher frequencies for locations closer to the mouth of the injector. This points to the sixteen- to twenty-two-points-per-wavelength spacing being sufficient for Loci-CHEM to capture those frequencies.

3.2.3 Mode Determination

The FFT results also gave information about the relative phases of frequencies in the pressure time histories. Pressure signals between locations could be in phase or out of phase with one another. Table 3.6 shows the difference in peak frequency phase angles between the reference transducer (location 1) and the other transducer locations (6, 7, and 8). Because of the spatial arrangement of the probe locations (Figure 1.1), possible radial modes could be seen by looking at the relative phase angle at location 6. Similarly, longitudinal modes could be seen by looking at the relative phase angles at locations 7 and 8.

Location 6 led location 1 about 178°at 2132 Hz. This phase difference indicated that 6 and 1 were out of phase with each other. Since 6 was located at approximately half the chamber radius and 1 on the chamber wall, the phase difference suggested a possible radial mode.

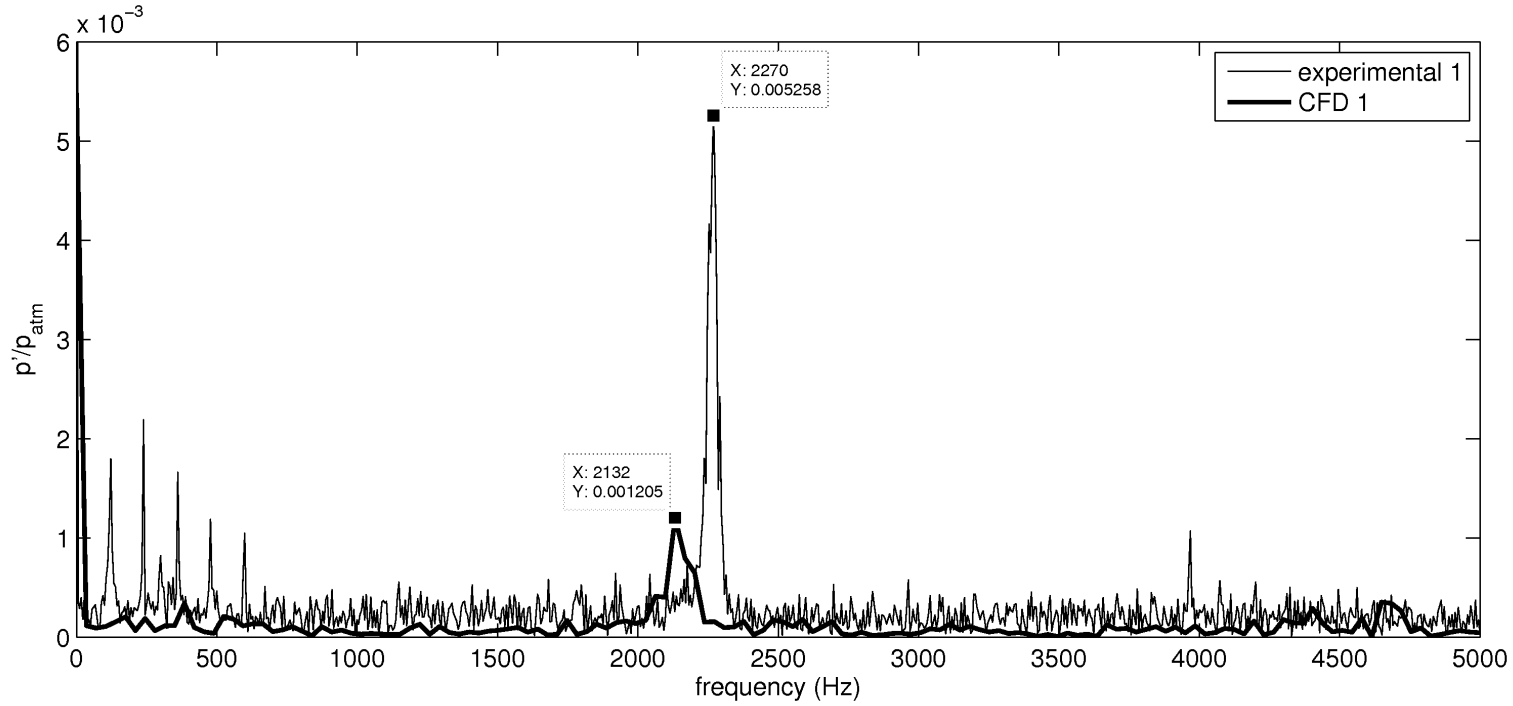

Figure 3.16: FFT of pressure fluctuations at 50.8 mm from the center of the injector on the fireface for the CFD and experimental results

Table 3.6: Relative phase angles at the dominant frequency

	Phase angle relative to Transducer 1	
Transducer	CFD (2132 Hz)	Experiment (2270 Hz)
6	178°	-155°
7	3.6°	12°
8	-12.3°	21.5°

The phase differences for locations 7 and 8 were within 15°of location 1, which indicated all three locations were in phase for that frequency. Since the magnitudes of 1, 7, and 8 were similar in the CFD results, a longitudinal mode was not likely present at that frequency.

As seen in Table 3.6, the phase angles at the dominant frequencies were similar in that locations 1 and 6 have a separation of greater than 150°. Though location 6 lead 1 in the CFD results but lagged 1 in the experiment, 6 and 1 were out of phase in both cases. This grouping of phase angles is indicative of a radial mode for both the experimental and CFD work. Coupled with the frequency strength results, this gave strong evidence that the CFD analysis was able to capture the same R1 mode seen in experiments at the same flow conditions.

The R1 pressure field configuration has its strongest antinode at the injector face. Since the pressure pressure difference between the injector inlet and the injector face strongly effect the velocity of propellant flowing from the injector, the pressure fluctuations at the injector face lead to fluctuations in the flow field at the same frequency. These flow field fluctuations then lead to fluctuations in the chemical

composition in the combustion region. The fluctuating heat release from combustion further encourages the chamber pressure fluctuations at the R1 frequency. Thus, the chamber pressure fluctuations coupled to fluctuations in the combustion region through the R1 mode.

CHAPTER 4

CONCLUSIONS

4.1 Concluding Remarks

In this work, a single-element rocket injector experiment [9] was modeled in the Loci-CHEM CFD code. The experiment was designed to characterize the injector-chamber coupling which produces the potentially destructive phenomenon of high-frequency combustion instabilities. A shear-coaxial injector was aligned with the center of the open cylindrical chamber and modeled as axisymmetric in CFD. A set of propellant flow conditions for this configuration from experiments was simulated using a single-step methane-oxygen combustion reaction and a hybrid RANS/LES model. The pressure data were compared between the experiment and CFD to identify the dominant frequencies excited by the unsteady combustion in that acoustic environment.

The strongest frequency found in the CFD analysis (2132 Hz) reproduced the experimental frequency within 150 Hz or 6 percent and corresponded to the R1 mode. The difference in frequencies was likely due to lower chamber temperatures in the CFD results. This difference in temperature may be due to accumulated heating from long operation of the experimental apparatus or external temperatures being

higher than those assumed for the CFD analysis. The magnitude of the fluctuations was much less in the CFD results than the experimental data. Relative phase angles between the reference location and the other transducer locations appeared similar to the experimental results.

4.2 Recommendations

Future studies should extend beyond axisymmetric simulations to model a full experimental chamber. This would allow three-dimensional turbulent structures to be captured. Additionally, simulations could be conducted with the injector placed off-axis in the chamber, as in the basis experiments. These placements would allow excitation of additional chamber modes not available in the chamber-centered configuration. Also, upstream turbulence could be introduced to see what effects this would have on the strength of fluctuations in the chamber. However, this might require additional boundary conditions to be implemented which were not available in the Loci-CHEM version used in this work. The effects of intermediate species and radicals on the unsteady phenomena could be studied by using more detailed reaction mechanisms.

APPENDICES

APPENDIX A

NATURAL FREQUENCIES IN CYLINDRICAL CHAMBER

The natural frequencies of a cylindrical chamber may be derived from linear acoustic theory [15]. Let $p' = p - \langle p \rangle_T$ be the pressure fluctuation above the local, time-averged pressure $\langle p \rangle_T$. Assuming only small fluctuations, viscosity and non-linear effects may be neglected. In such cases, the linear, lossless acoustic wave equations governs pressure fluctuation:

$$\nabla^2 p' = \frac{1}{a^2} \frac{\partial^2 p'}{\partial t^2} \tag{A.1}$$

For cylindrical coordinates,

$$\nabla^2 = \frac{1}{r} \frac{\partial}{\partial r} \left(r \frac{\partial}{\partial r} \right) + \frac{1}{r^2} \frac{\partial^2}{\partial \theta^2} + \frac{\partial^2}{\partial z^2}. \tag{A.2}$$

Letting

$$p' = p e^{i\omega t} \tag{A.3}$$

where p is the magnitude of p'. Then,

$$p'(r,\theta,z,t) = p(r,\theta,z)e^{i\omega t}. \tag{A.4}$$

From here, (A.1) becomes,

$$e^{i\omega t}\nabla^2 p = -\frac{\omega^2}{a^2}e^{i\omega t}p = -k^2 e^{i\omega t}p \tag{A.5}$$

or

$$\nabla^2 p + k^2 p = 0. \tag{A.6}$$

This may be solved using separation of variables by letting $p(r,\theta,z) = R(r)\Theta(\theta)Z(z)$. Then, (A.6) becomes

$$\Theta Z\frac{1}{r}\frac{d}{dr}\left(r\frac{dR}{dr}\right) + RZ\frac{1}{r^2}\frac{d^2\Theta}{d\theta^2} + R\Theta\frac{d^2Z}{dz^2} + k^2 R\Theta Z = 0. \tag{A.7}$$

Assuming temperature to be relatively uniform, k is constant. Multipying by $\frac{r^2}{R\Theta Z}$ yields

$$\frac{r}{R}\frac{d}{dr}\left(r\frac{dR}{dr}\right) + \frac{1}{\Theta}\frac{d^2\Theta}{d\theta^2} + \frac{r^2}{Z}\frac{d^2Z}{dz^2} + r^2k^2 = 0. \tag{A.8}$$

Inspection shows that this may be split into two independant parts which must equal a constant:

$$\frac{r}{R}\frac{d}{dr}\left(r\frac{dR}{dr}\right) + \frac{r^2}{Z}\frac{d^2Z}{dz^2} + r^2k^2 = -\frac{1}{\Theta}\frac{d^2\Theta}{d\theta^2} = m^2. \tag{A.9}$$

Then,

$$\frac{d^2\Theta}{d\theta^2} = -\Theta m^2, \tag{A.10}$$

and (A.9) may be further separated such that

$$\frac{1}{rR}\frac{d}{dr}\left(r\frac{dR}{dr}\right) - \frac{m^2}{r^2} + k^2 = -\frac{1}{Z}\frac{d^2Z}{dz^2} = k_{zl}^2. \tag{A.11}$$

Thus,

$$\frac{d^2Z}{dz^2} = -Zk_{zl}^2. \tag{A.12}$$

Finally, letting

$$k^2 = k_{mn}^2 + k_{zl}^2, \tag{A.13}$$

and multiplying (A.11) by Rr^2 yields

$$r\frac{dR}{dr} + r^2\frac{d^2R}{dr^2} + (k_{mn}^2 r^2 - m^2)R = 0. \tag{A.14}$$

Thus, for pressure fluctuations in cylindrical coordinates, three ordinary differential equations need to be solved which are linked through the constants m,k_{mn}, and k_{zl}: (A.10), (A.12), and (A.14). These yield the solutions

$$Z = \cos k_{zl} z \tag{A.15a}$$

$$\Theta = \cos m\theta \tag{A.15b}$$

$$R = J_m(k_{mn} r) \tag{A.15c}$$

Since $\Theta(\theta) = \Theta(\theta+2\pi)$, m must be an integer ($m = 0, 1, 2, \ldots$). For a chamber of length L and a radius of r_w,

$$\left(\frac{\partial P}{\partial z}\right)_{z=0} = \left(\frac{\partial P}{\partial z}\right)_{z=L} = \left(\frac{\partial P}{\partial r}\right)_{r=r_w} = 0, \tag{A.16}$$

and the solution pressure must be finite. Then, $k_{zl} = \dfrac{l\pi}{L}$, where $l = 0, 1, 2, \ldots$, and $k_{mn} = \dfrac{j'_{mn}}{r_w}$ where j'_{mn} is the nth extremum of the mth Bessel function of the first kind. Thus, from (A.5) and (A.13) the natural frequencies of the chamber are found to be

$$f_{lmn} = \frac{a}{2\pi}\sqrt{\left(\frac{j'_{mn}}{r_w}\right)^2 + \left(\frac{l\pi}{L}\right)^2}, \tag{A.17}$$

where l, m, and n are the integer mode numbers for the longitudinal, tangential, and radial directions, respectively.

APPENDIX B

LOCI-CHEM CASE SETUP FILES

The following files were used in the final steps of the analysis of the experiment [9]. Loci-CHEM requires a case setup and methods file (Section B.1), a chemical reactions file (Section B.2), and a transport properties file (Section B.3) [17].

B.1 Vars File

```
// coax burner description file
// modified from example file included with CHEM
{
//initialConditionsFile: ic.dat
grid_file_info: <Lref=1m> //
boundary_conditions: <
   BC_1=fixedMass(mdot=1.816667e-6 kg/s,T0=295,mixture=[O2=1.0]),//
      ...oxidizer entrance
   BC_2=fixedMass(mdot=3.619444e-6 kg/s,T0=295,mixture=[CH4=0.27,N2
      ...=0.73]),// fuel entrance
   BC_3=viscousWall(adiabatic),// fuel/oxidizer wall
   BC_4=viscousWall(adiabatic),// Outer fuel wall
   BC_7=viscousWall(adiabatic),// Chamber wall
   BC_8=farfield(p=1 atm, T=295.0K,u=0.0m/s),// open top
   BC_9=symmetry,
   BC_10=symmetry>

// requisite initial conditions
ql     : <p=1.01325e5,T=295.0,u=0.0> //x<0
qr     : <p=1.01325e5,T=295.0,u=0.0> //x>0

// reaction model
chemistry_model: CH4air_5s1r

transport_model: chemkin
diffusion_model: chemkin
```

```
dtmax:  2e-7

print_freq: 500
probe_freq: 1
plot_modulo: 0
plot_freq: 500
restart_modulo: 0
restart_freq: 2000
stop_iter: 200000

// This is an unsteady calculation, use newton iterations
newton_iter: 3
gauss_seidel_iter: 4
time_integration: euler

limiter: barth
turbulence_model: SST
multi_scale: LES //for hybrid RANS/LES mode
plot_output: vort_mag

}
```

B.2 Chemistry File

```
// One-step methane air reaction
// from Coffee
species = {
CH4 ;
O2 : <mf = 0.233 > ;
N2 : <mf = 0.767 > ;
CO2 ;
H2O ;
} ;

// Kf needs to have units of m^6/Kmole^2-sec
reactions = {
CH4 + 2 O2  -> CO2 + 2 H2O   = <Kf = Arrhenius(1.0342e15, 0.0, 1.464e4)
    ...> ;
} ;
```

B.3 Transport Properties File

```
 //Species transport data file
 //
species_count =     5
 //
 species : CH4              O2               N2               CO2
 H2O
```

```
 //
number_order =      4
 //
 patmos =     1.000000000000000
 //
 //Molecular weights
    16.04303000000000        31.99880000000000        28.01340000000000
    44.00995000000000        18.01534000000000
 //
 //Conductivity coefficients
 //
   -8.874382344320916        5.444578869363071       -0.5503965309890945
   2.1227547834363151E-02   -2.128586669891020         2.989595803958899
  -0.2874003348565147        1.2408060363915058E-02    7.599031319456215
   -1.179842906217822        0.3029785257440284       -1.5390342142501694E
      ...-02
   -14.00155575656455        7.062907492366090        -0.7437411127449518
   2.8947153276796398E-02    16.28736883790506        -5.894936320836811
    1.088693741277774       -5.5068483982513350E-02
 //
 //Viscosity coefficients
 //
   -18.59562801064127        2.942564248328408        -0.2951678865515794
   1.2624547733706337E-02   -16.02272304619687         2.173984407478319
  -0.1980864700722431        8.5386042679240267E-03   -15.54301224147343
    1.934049642275035       -0.1673657315886495        7.2282516744803906E
      ...-03
   -22.71607688806846        4.577093709251384        -0.4916100949153130
   2.0499283416514118E-02   -14.94019979115564         0.5607251520099196
   0.1374631390185346       -1.0371109583235267E-02
 //
 //Diffusion coefficients
 //
   -16.52951824779096        3.843617175568197        -0.2778105455935267
   1.1747191369615462E-02   -15.86034385007461         3.587002561822792
  -0.2469118727888828        1.0506747923792832E-02   -15.59372249140550
    3.485035001905756       -0.2346047927985672        1.0012158324175428E
      ...-02
   -18.55417266062302        4.475279941504397        -0.3519216583183169
   1.4641227828256798E-02   -20.62417143816724         5.237759630215725
  -0.4271920051058041        1.7008774568781658E-02   -15.86034385007461
    3.587002561822792       -0.2469118727888828        1.0506747923792832E
      ...-02
   -15.06607132321907        3.251703011852207        -0.2050415091514286
   8.7632156693108736E-03   -14.75677534948236         3.131587188228075
  -0.1897192316558912        8.1115895593764191E-03   -17.69026495608682
    4.126589155450874       -0.3113244857850248        1.3069498472979326E
      ...-02
   -20.24191975308118        5.144079912715197        -0.4226803628374081
   1.7095173427748363E-02   -15.59372249140550         3.485035001905756
  -0.2346047927985672        1.0012158324175428E-02   -14.75677534948236
    3.131587188228075       -0.1897192316558912        8.1115895593764191E
      ...-03
   -14.53138430792167        3.046809042716508        -0.1793674003177416
```

7.6902609799830981E−03 −17.46777551543542 4.052550394325762
−0.3030621626670672 1.2764799828276338E−02 −20.05452866247267
5.086759803776036 −0.4179720879357015 1.6995346462791522E
...−02
−18.55417266062302 4.475279941504397 −0.3519216583183169
1.4641227828256798E−02 −17.69026495608682 4.126589155450874
−0.3113244857850248 1.3069498472979326E−02 −17.46777551543542
4.052550394325762 −0.3030621626670672 1.2764799828276338E
...−02
−20.32277074775620 4.940108249146012 −0.4030384063360874
1.6505526676198690E−02 −20.35198019564506 4.848907205636675
−0.3561695511694323 1.3189222509157281E−02 −20.62417143816724
5.237759630215725 −0.4271920051058041 1.7008774568781658E
...−02
−20.24191975308118 5.144079912715197 −0.4226803628374081
1.7095173427748363E−02 −20.05452866247267 5.086759803776036
−0.4179720879357015 1.6995346462791522E−02 −20.35198019564506
4.848907205636675 −0.3561695511694323 1.3189222509157281E
...−02
−15.27660467573957 2.429358167262868 2.0005836177121629E
...−02
−5.0758223641027391E−03

REFERENCES

[1] Terence P. Coffee, Anthony J. Kotlar, and Martin s. Miller. The overall reaction concept in premixed, laminar, steady-state flames. i. stoichiometrics. *Combustion and Flame*, 54(1-3):155–169, December 1983.

[2] G.P. Sutton and O. Biblarz. *Rocket Propulsion Elements*. John Wiley and Sons, 2001.

[3] R.C. Cavitt, R.A. Frederick, and V.G. Bazarov. Laboratory scale survey of pentad injector stability characteristics. *Journal of Propulsion and Power*, 24(3):534–540, 2008.

[4] R.E. Byrd and R.A. Frederick. Instability characteristics of a gaseous-oxygen/methane pentad injector. *Journal of Propulsion and Power*, 26(4):689–695, Jul-Aug 2010.

[5] H.H Huynh, B. Sweeney, and R.A. Frederick. Mode assessment of a single-element shear coaxial injector. In *45th AIAA/ASME/SAE/ASEE Joint Propulsion Conference*, August 2009.

[6] C.E. Dexter et al. Scaling techniques for design, development, and test. In V. Yang et al., editors, *Liquid Rocket Thrust Chamber: Aspects of Modeling Analysis, and Design*, volume 200 of *Progress in Astronautics and Aeronautics*, pages 553–600. AIAA, Reston, VA, 2004.

[7] M.L. Dranovsky et al. Combustion instabilities in liquid rocket engines: Testing and development practices in russia. volume 201 of *Progress in Astronautics and Aeronautics*, pages 171–190. AIAA, 2007.

[8] C.H. Sohn et al. Hot-fire injector test for determination of combustion stability boundaries using model chamber. *Journal of Mechanical Science and Technology*, 19(9):1821–1832, 2005.

[9] Huy Huynh. Mode assessment of a single-element shear-coaxial injector. Master's thesis, UAHuntsville, 2009.

[10] R. Jensen, H. Dodson, and S. Claflin. Lox/hydrocarbon combustion instability investigation. Technical report, Rockwell International: Rocketdyne Division, Canoga Park, CA, Jul 1989.

[11] Emre Sozer, Aravind Vaidyanathan, Corin Segal, and Wei Shyy. Computational assessment of gaseous reacting flows in single element injector. In *47th AIAA Aerospace Sciences Meeting including The New Horizons Forumn and Aerospace Exposition*, Orlando, Florida, January 2009.

[12] Chenzhou Lian and Charles L. Merkle. Contrast between steady and time-averaged unsteady combustion simulations. *Computers and Fluids*, 44(1):328–338, May 2011.

[13] Randolph Jedediah Smith. *Computational Investigations of High Frequency Acoustics and Instabilities in a Single-Element Rocket Combustor*. Ph.D. dissertation, Purdue University, 2010.

[14] Michael J. Nusca. Modeling combustion instability in small mmh-nto liquid rocket engines using cfd: Injector-chamber coupling. In *48th AIAA Aerospace Sciences Meeting including The New Horizons Forumn and Aerospace Exposition*, Orlando, Florida, January 2010.

[15] Lawrence E. Kinsler, Austin R. Frey, Alan B. Coppens, and James V. Sanders. *Fundamentals of Acoustics*. Wiley, 4th edition, 2009.

[16] T. J. Chung. *General Continuum Mechanics*. Cambridge, 2nd edition, 2007.

[17] E.A. Luke and et al. *CHEM 3: A Finite-Rate Viscous Chemistry Solver The User Guide*. SimCenter at Mississippi State University, October 2006. Distributed with Loci-CHEM.

[18] J. Gaither, D. Marcum, and B. Mitchell. Solidmesh: A solid modeling approach to unstructured grid generation. In *7th International Conference on Numerical Grid Generation in Computational Field Simulations*, 2000.

[19] David L. Marcum and Nigel P. Weatherill. Unstructured grid generation using iterative point insertion and local reconnection. *AIAA Journal*, 33(9):1619–1625, September 1995.

[20] C.J. Roy and et al. Verification of rans turbulence models in loci-chem using the method of manufactured solutions. In *18th AIAA Computational Fluid Dynamics Conference*, Miami, FL, June 2007.

[21] C.K.W. Tam and J.C Webb. Dispersion-relation-preserving finite difference schemes for computational acoustics. *Journal of Computational Physics*, 107:262–281, 1993.

[22] Scott B. Tashakkor. Application of the loci-based discontinuous galerkin method to acoustics. Master's thesis, UAHuntsville, 2008.

[23] Aditi Saxena. Interaction of a premixed flame with an acoustic disturbance. Master's thesis, UAHuntsville, 2004.

[24] Caroline P. Hood. A two-dimensional cartesian and axisymmetric study of combustion-acoustic interaction. Master's thesis, UAHuntsville, 2006.

[25] Abdelkader Frendi and Merwin Sibulkin. Dependence of minimum ignition energy on igition parameters. *Combustion Science and Technology*, 73:395–413, 1990.

[26] Lieuwen T. Natarajan, J. and J. Seitzman. Laminar flame speeds of h2/co mixtures: Effect of co2 dilation, preheat temperature, and pressure. *Combustion and Flame*, 151:104–119, 2007.

[27] Chen Dong, Qulan Zhou, Qinxin Zhao, Yaqing Zhang, Tongmo Xu, and Shien Hui. Experimental study on the laminar flame speed of hydrogen/carbon monoxide/air mixtures. *Fuel*, 88:1858–1863, 2009.